eNeuro

Research Article: New Research

Novel Tools and Methods

Neuronal Cascades Shape Whole-Brain Functional Dynamics at Rest

Giovanni Rabuffo, Jan Fousek, Christophe Bernard,* and Viktor Jirsa*

https://doi.org/10.1523/ENEURO.0283-21.2021

Aix Marseille University, INSERM, INS, Institut de Neurosciences des Systèmes, 13005 Marseille, France

Visual Abstract

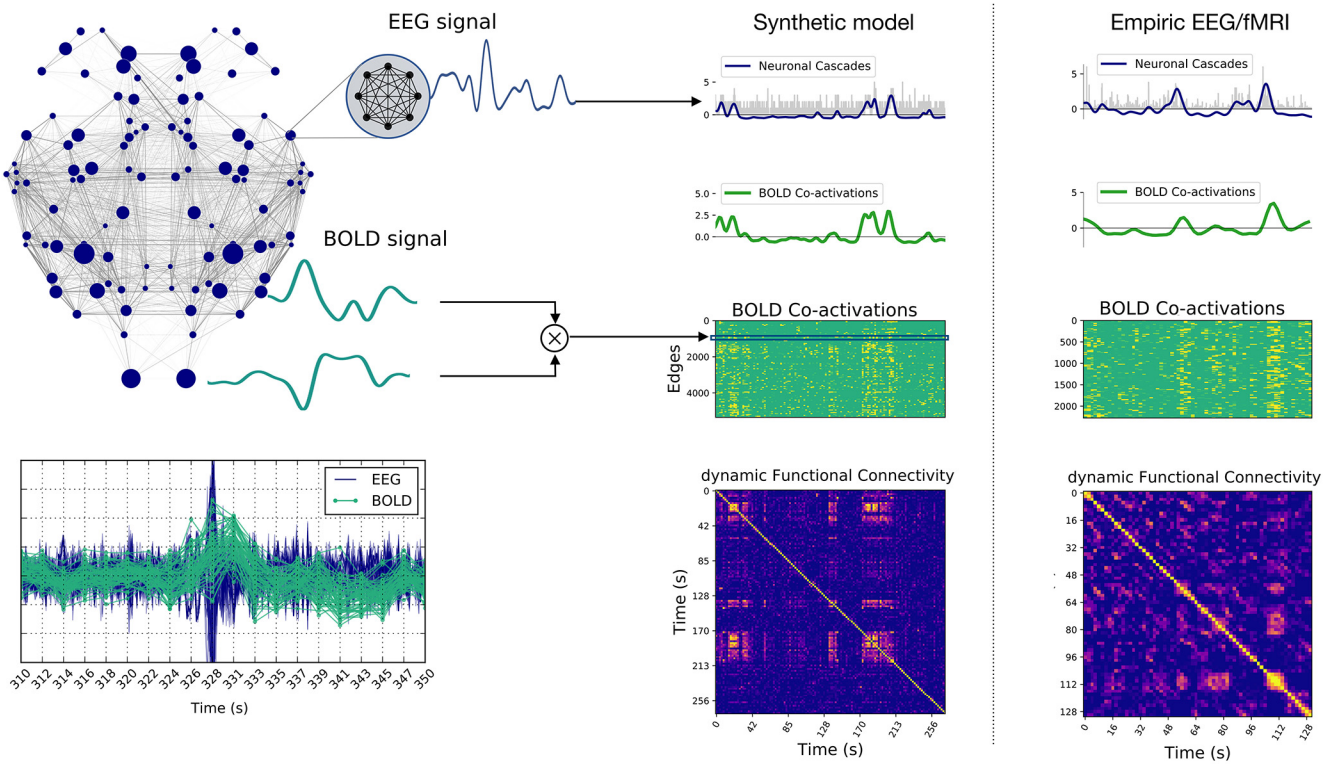

Significance Statement

Functional connectivity (*FC*) and its dynamics are widely used as a proxy of brain function and dysfunction. Their neuronal underpinnings remain unclear. Using connectome-based modeling, we link the fast temporal microscopic neuronal scale to the slow emergent whole-brain dynamics. We show that cascades of neuronal activations spontaneously propagate in resting state-like conditions. The largest neuronal cascades result in the co-fluctuation of blood oxygen level-dependent (BOLD) signals at pairs of brain regions, which in turn translate to stable brain states. Thus, we provide a theoretical framework for the emergence and the dynamics of resting-state networks (*RSNs*). We verify these predictions in empirical mouse functional magnetic resonance imaging (fMRI) and human EEG/fMRI datasets measured in resting states conditions. Our work sheds light on the multiscale mechanisms of brain function.

At rest, mammalian brains display remarkable spatiotemporal complexity, evolving through recurrent functional connectivity (*FC*) states on a slow timescale of the order of tens of seconds. While the phenomenology of the resting state dynamics is valuable in distinguishing healthy and pathologic brains, little is known about its underlying mechanisms. Here, we identify neuronal cascades as a potential mechanism. Using full-brain network modeling, we show that neuronal populations, coupled via a detailed structural connectome, give rise to large-scale cascades of firing rate fluctuations evolving at the same time scale of resting-state networks (*RSNs*). The ignition and subsequent propagation of cascades depend on the brain state and connectivity of each region. The largest cascades produce bursts of blood oxygen level-dependent (BOLD) co-fluctuations at pairs of regions across the brain, which shape the simulated *RSN* dynamics. We experimentally confirm these theoretical predictions. We demonstrate the existence and stability of intermittent epochs of *FC* comprising BOLD co-activation (CA) bursts in mice and human functional magnetic resonance imaging (fMRI). We then provide evidence for the existence and leading role of the neuronal cascades in humans with simultaneous EEG/fMRI recordings. These results show that neuronal cascades are a major determinant of spontaneous fluctuations in brain dynamics at rest.

Key words: EEG/fMRI; network modeling; neuronal cascades; resting state

Introduction

At rest, functional magnetic resonance imaging (fMRI) reveals the existence of periods during which blood oxygen level-dependent (BOLD) activity is highly correlated between specific brain regions, known as resting-state networks (*RSNs*). *RSNs* are consistently observed across several mammalian species including humans (Fox and Raichle, 2007; Power et al., 2011) and non-human (Vincent et al., 2007) primates, as well as in rats (Upadhyay et al., 2011; Lu et al., 2012) and mice (Sforazzini et al., 2014; Stafford et al., 2014; Gozzi and Schwarz, 2016; Grandjean et al., 2020). Functional connectivity (*FC*) can be used to characterize these strongly correlated functional communities of brain network nodes. A growing body of research on mammalian species emphasizes the dynamic nature of *RSNs*, showing that large-scale *FC* patterns switch between stable and unstable epochs at an infraslow pace ($<$0.1 Hz; Tagliazucchi et al., 2012b; Allen et al., 2014; Qin et al., 2015; Hindriks et al., 2016; Grandjean et al., 2017; Preti and Van De Ville, 2017; Gonzalez-Castillo and Bandettini, 2018). Dynamic *FC* (*dFC*; Hutchison et al., 2013) measures *FC* fluctuations and provides a marker of healthy, aging, and diseased brains (Damaraju et al., 2014; Rashid et al., 2014; Su et al., 2016; Du et al., 2017; Preti et al., 2017; Battaglia et al., 2020). Our current understanding of these phenomena rests on computational studies, performed at the whole-brain level, suggesting that the *RSN* dynamics is an emergent property of the network (Ponce-Alvarez et al., 2015), which operates near criticality (Ghosh et al., 2008; Deco and Jirsa, 2012; Jirsa et al., 2017). Nevertheless, the range of possible mechanistic underpinnings remains vast and requires further narrowing down. Here, we address this issue and investigate *in silico* the potential neuronal mechanisms giving rise to whole-brain network dynamics, generate predictions and test them *in vivo*. We use The Virtual Brain (TVB), a neuroinformatics and simulation platform, which allows connectome-based whole-brain modeling of multiple species including humans (Sanz-Leon et al., 2015) and mice (Melozzi et al., 2017). TVB includes a fixed number of network nodes (at least one per brain region) and the physical connections that link them, such as white matter tracts defined by diffusion tensor imaging or axon projections obtained with virus injections (Sanz Leon et al., 2013). A large number of neural mass models (NMMs) are readily available in TVB, which produce activity of neuronal populations and map on a range of brain imaging modalities including BOLD fMRI, EEG, and MEG signals. We here adapt a novel NMM, which has been previously derived as the exact limit of an infinite number of all-to-all coupled quadratic integrate-and-fire (QIF) neurons (Montbrió et al., 2015; Fig. 1*A*). This analytic step allows to derive the average firing rate and membrane potential of a mesoscopic neuronal population, thus providing suitable neural mass variables while keeping track of the internal spiking neural network organization, which is important to infer potential mechanisms at the neuronal scale. Using this NMM, we report a mechanism by which spontaneous local re-organizations of regional spiking neural networks, can trigger global infra-slow fluctuations, which we name neuronal cascades. The largest neuronal cascades give rise to bursts of simulated BOLD co-activations (BOLD-CAs) at pairs of brain regions across the brain, which in turn account for stable long-lasting *FC* states and their dynamics. We verify experimentally the link between BOLD-CA and *dFC* in mouse fMRI and human EEG-fMRI. On the simultaneous human EEG acquisition, we discover the presence of neuronal cascades and we demonstrate their role in driving the switching behavior of *FC* states.

Received June 29, 2021; accepted September 15, 2021; First published September 27, 2021.

The authors declare no competing financial interests.

Author contributions: G.R., C.B., and V.J. designed research; G.R. and J.F. performed research; G.R. and J.F. analyzed data; G.R. and C.B. wrote the paper.

This work was supported by Agence Nationale de la Recherche (ANR) Grants ANR-17-CE37-0001-CONNECTOME and ANR-20-NEUC-0005-01-Brainstim and European Union (EU)'s EC | Horizon 2020 (EU Framework Programme for Research and Innovation) Grants 945539 (SGA3) and 826421, and Israeli-French high council for scientific & technological research program (Maïmonide).

*C.B. and V.J. are equally contributing last authors.

Correspondence should be addressed to Giovanni Rabuffo at giovanni.rabuffo@univ-amu.fr.

https://doi.org/10.1523/ENEURO.0283-21.2021

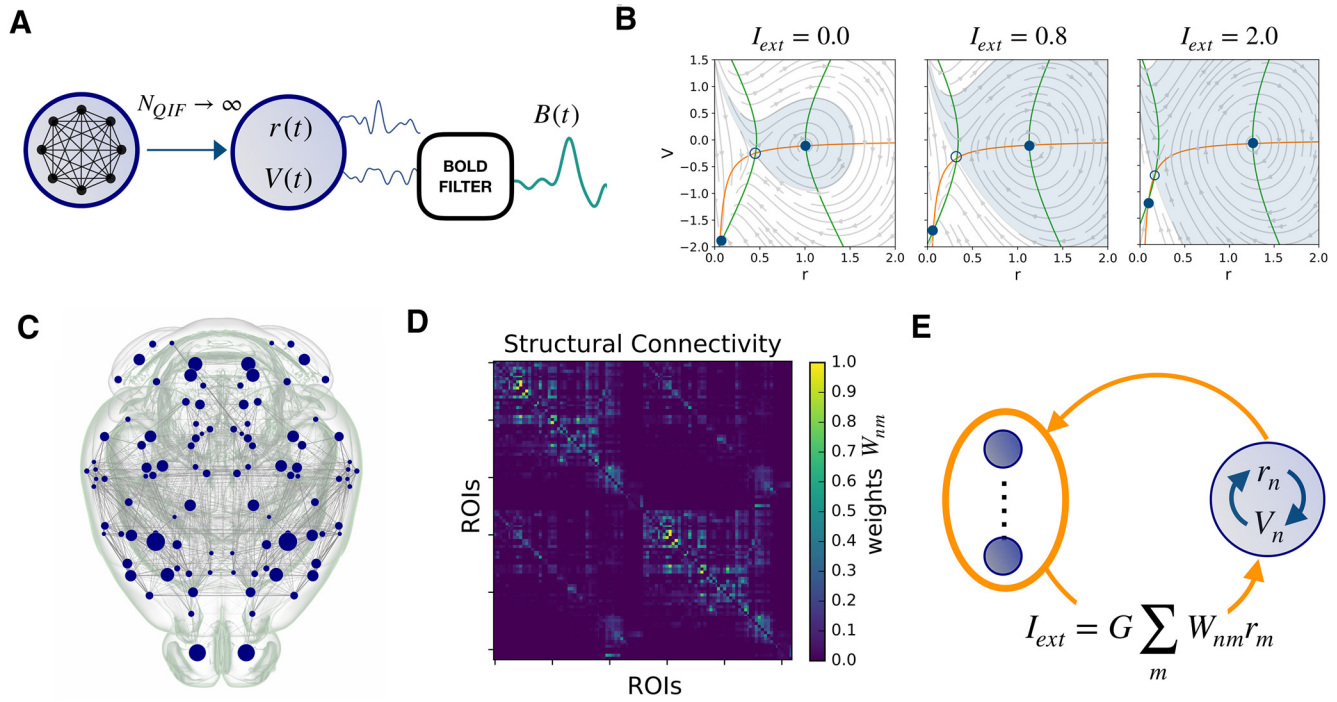

Figure 1. Connectome based modeling. ***A***, The mean firing rate r and membrane potential V variables of the NMM are derived as the limit of infinite all-to-all coupled QIF neurons. Applying the Balloon–Windkessel model to $V_n(t)$ we obtain the simulated BOLD signal $B_n(t)$ at node n. ***B***, The phase plane of each decoupled node ($I_{ext} = 0$) has a "down" stable fixed point and an "up" stable focus (full dots). These points are defined at the intersection of the nullclines $\dot{r} = 0$ (orange line) and $\dot{V} = 0$ (green line) where the dynamics freezes. The empty circle marks an unstable fixed point. As the external current I_{ext} is increased, the phase plane of the neural mass changes (see equations in Materials and Methods). In particular, the basin of attraction of the up state gradually becomes larger than that of the down state, while the fixed points move farther apart. ***C***, ***D***, The mouse connectome and structural connectivity W_{nm} were imported from the tracer experiments of the Allen Institute. The 104 cortical ROIs (corresponding to network nodes) are specified in Table 1. ***E***, When the regions are coupled in a brain network, each node n receives an input current I_{ext} which is the sum of the other nodes' firing rates, weighted by the structural connectivity. According to panel ***B***, this input provokes a distortion of the local phase plane at node n.

These findings provide the first evidence of a multiscale mechanism underlying *RSN* dynamics which can be robustly assessed in non-invasive brain imaging signals.

Materials and Methods

Empirical mouse connectome

The connectome used for the simulations was extracted using The Virtual Mouse Brain pipeline described previously (Melozzi et al., 2017), which processes the tracer experiments performed at the Allen Institute (Oh et al., 2014). There, adult male C57Bl/6J mice are injected in specific brain regions with a recombinant adeno-associated virus, which expresses the EGFP anterograde tracer. In each experiment, the tracer migration signal is detected by a serial two-photon tomography system. The anterograde tracing provides information about the axonal projections starting at the injected site. We define the injection density of the source region as the number of infected pixels normalized by the total number of pixels in the region. Similarly, the projection density is defined in every region as the number of pixels detected in the target region following an injection at the source, normalized by the total number of pixels belonging to the target region. The tracer-based connectome is built by averaging over injection experiments performed in the right brain areas and targeting regions in ipsilateral and contralateral hemispheres. Through the Allen Connectivity Builder interface in TVB we parceled the brain in 104 anatomic regions of interest (ROIs; Table 1). Then, we defined the connection strength between source region n and target region m, i.e., the structural edge nm, as the ratio between the projection density at m and the injection density at n. The tracer structural connectome W, with edges normalized between 0 and 1 is shown in Figure 1*D*.

Neural mass model

The dynamics of a brain ROIs (i.e., a node in the structural network) is described by a NMM derived analytically as the limit of infinitely all-to-all coupled θ-neuron phase oscillators, whose dynamics is equivalent to that of QIF neurons (Fig. 1*A* ; Montbrió et al., 2015). The i-th neuron is described by the equation

$$\tau_c \dot{V}_i(t) = V_i^2(t) + \eta_i + J\bar{s}(t) + I(t)$$
$$\text{if} \quad V_i \geq V_p \quad \text{then} \quad V_r \leftarrow V_i. \qquad (1)$$

As the membrane potential reaches a peak value V_p, it resets to V_r. The limit $V_p = -V_r \to \infty$ is considered. The

Table 1: List of brain ROIs of the Allen Mouse Atlas considered in the simulations

ROI ID:	ROI name:	ROI ID:	ROI name:
0	Right primary motor area	52	Left primary motor area
1	Right secondary motor area	53	Left secondary motor area
2	Right primary somatosensory area, nose	54	Left primary somatosensory area, nose
3	Right primary somatosensory area, barrel field	55	Left primary somatosensory area, barrel field
4	Right primary somatosensory area, lower limb	56	Left primary somatosensory area, lower limb
5	Right primary somatosensory area, mouth	57	Left primary somatosensory area, mouth
6	Right primary somatosensory area, upper limb	58	Left primary somatosensory area, upper limb
7	Right supplemental somatosensory area	59	Left supplemental somatosensory area
8	Right gustatory areas	60	Left gustatory areas
9	Right visceral area	61	Left Visceral area
10	Right dorsal auditory area	62	Left dorsal auditory area
11	Right primary auditory area	63	Left primary auditory area
12	Right ventral auditory area	64	Left ventral auditory area
13	Right primary visual area	65	Left primary visual area
14	Right anterior cingulate area, dorsal part	66	Left anterior cingulate area, dorsal part
15	Right anterior cingulate area, ventral part	67	Left anterior cingulate area, ventral part
16	Right agranular insular area, dorsal part	68	Left agranular insular area, dorsal part
17	Right retrosplenial area, dorsal part	69	Left retrosplenial area, dorsal part
18	Right retrosplenial area, ventral part	70	Left retrosplenial area, ventral part
19	Right temporal association areas	71	Left temporal association areas
20	Right perirhinal area	72	Left perirhinal area
21	Right ectorhinal area	73	Left ectorhinal area
22	Right main olfactory bulb	74	Left main olfactory bulb
23	Right anterior olfactory nucleus	75	Left anterior olfactory nucleus
24	Right piriform area	76	Left piriform area
25	Right cortical amygdalar area, posterior part	77	Left cortical amygdalar area, posterior part
26	Right field CA1	78	Left field CA1
27	Right field CA3	79	Left field CA3
28	Right dentate gyrus	80	Left dentate gyrus
29	Right entorhinal area, lateral part	81	Left entorhinal area, lateral part
30	Right entorhinal area, medial part, dorsal zone	82	Left entorhinal area, medial part, dorsal zone
31	Right subiculum	83	Left subiculum
32	Right caudoputamen	84	Left caudoputamen
33	Right nucleus accumbens	85	Left nucleus accumbens
34	Right olfactory tubercle	86	Left olfactory tubercle
35	Right substantia innominata	87	Left substantia innominata
36	Right lateral hypothalamic area	88	Left lateral hypothalamic area
37	Right superior colliculus, sensory related	89	Left superior colliculus, sensory related
38	Right inferior colliculus	90	Left inferior colliculus
39	Right midbrain reticular nucleus	91	Left midbrain reticular nucleus
40	Right superior colliculus, motor related	92	Left superior colliculus, motor related
41	Right periaqueductal gray	93	Left periaqueductal gray
42	Right pontine reticular nucleus, caudal part	94	Left pontine reticular nucleus, caudal part
43	Right pontine reticular nucleus	95	Left pontine reticular nucleus
44	Right intermediate reticular nucleus	96	Left intermediate reticular nucleus
45	Right central lobule	97	Left central lobule
46	Right culmen	98	Left culmen
47	Right simple lobule	99	Left simple lobule
48	Right ansiform lobule	100	Left ansiform lobule
49	Right paramedian lobule	101	Left paramedian lobule
50	Right copula pyramidis	102	Left copula pyramidis
51	Right paraflocculus	103	Left paraflocculus

parameter η_i is the neuron excitability, and it enters as an heterogeneous current in the membrane potential. A time-dependent current $I(t)$ homogeneously affects all the neurons in the neural mass. The synaptic activation $s(t)$ of a single neuron respects the equation $Q \cdot s(t) = \sum_k \delta(t - t_k)$, being $Q = (1 - \tau \frac{d}{dt})$ and t_k the arrival time of the presynaptic action potential. The neuronal coupling among N_{QIF} neurons inside a neural mass is given by the average synaptic activation $\bar{s}(t) = \frac{1}{N_{QIF}} \sum_{j>1}^{N_{QIF}} s(t)$ scaled by the synaptic weight J. Assuming a Lorentzian distribution of the membrane potentials across the coupled neuronal population it is possible to perform the $N_{QIF} \to \infty$ limit exactly according to the Ott–Antonsen ansatz (Ott and Antonsen, 2008). Also, the heterogeneous currents are distributed according to a

Lorentzian distribution with width at mid-height Δ and peak location η. After the limit we can describe the activity in a neural mass n in terms of the average membrane potential $V_n(t)$ and the average firing rate $r_n(t)$ (which corresponds to $\bar{s}(t)$ in the limit $\tau \to 0$). The dynamics associated with a local network node is then described by the following NMM equations:

$$\tau_c \dot{r}_n(t) = \frac{\Delta}{\pi} + 2r_n(t)V_n(t), \quad (2)$$

$$\tau_c \dot{V}_n(t) = V_n^2(t) + \eta + Jr_n(t) - \pi^2 r_n^2(t) + I(t). \quad (3)$$

The synaptic weight $J = 14.5$, the average neuronal excitability $\eta = -4.6$, the spread of the heterogeneous noise distribution $\Delta = 0.7$, and the characteristic time $\tau_c = 1$ are homogeneously tuned so that each decoupled node is in a bistable regime with a "down" fixed point and an "up" stable focus in the 2D phase space (Fig. 1*B*, $I_{ext} = 0$). Differently from standard NMMs, the chosen model quantifies the internal amount of synchronization of the constituent neurons by preserving the analytic form of the Kuramoto parameter (Kuramoto, 2003)

$$Z_n(t) = |\sum_i \exp(i\theta_i)| = K_n(t)\exp(i\theta_n(t)), \quad (4)$$

during the thermodynamic limit. The phase-oscillator representation (i.e., in terms of θ_i) of the QIF equations can be achieved from Equation 1 by a change of variables $V_i = \tan(\theta_i/2)$. K_n and θ_n are the average amount of synchronization and the average phase of the neurons in the node n. The real and imaginary components of Z_n are connected to the average membrane potential V_n and firing rate r_n of the neural population n via the relation:

$$Z_n = \frac{1 - w_n^*}{1 + w_n^*}, \quad w_n \equiv \pi r_n + iV_n. \quad (5)$$

Connectome-based modeling

The local model is then coupled over an empirically extracted connectome (Fig. 1*C*,*D*). The coupling term enters as an additive current in the average membrane potential equations (see also Fig. 1*E*):

$$I(t) = G\sum_{m \neq n} W_{nm} r_m(t - \tau_{nm}). \quad (6)$$

The global coupling parameter G sets the impact of the connectivity matrix W_{nm} over the local dynamics. The time delay $\tau_{nm} = l_{nm}/v$ is given by the tract length between nodes n and m divided by the average conduction speed which we set to a realistic value $v = 4$ *m/s*. Since the firing rate is by definition greater than or equal to zero, all the interactions are excitatory.

The numeric integration of the nodal equations over the network is performed using TVB open-source neuroinformatics platform (Sanz Leon et al., 2013). The solution of the coupled system consists of a neuroelectric raw dataset describing the evolution of the variables $(r_n(t), V_n(t))$ in each region n of the connectome. These variables are our measure of microscopic activity. The sampling rate of these neuroelectric variables is set to 1000 Hz. The surrogate BOLD activity $B_n(t)$ in each region is derived by filtering the membrane potential with the Balloon–Windkessel model (Friston et al., 2000; default values implemented in TVB). We use a repetition time of 2 s so that the BOLD rate is 0.5 Hz.

Note that the conduction speed v is a function of the physical tract lengths l_{nm} of the empirical connectome and of the resolution Dt of the simulated signal, which physical interpretation is arbitrary. We impose it to be $Dt = 1$ ms. Accordingly, 2000 time steps correspond to 2 s = 1 BOLD point. All the dimensional arguments treated in the text are based on this convention. In particular, we adopted a nondimensional formalism for the NMM Equation 2, where only the characteristic time constant τ_c has the dimension of time.

Mouse and human empiric datasets

The empirical mouse fMRI dataset was imported from the publicly available collection Grandjean (2020). For our analysis, we used the cohort of 20 control wild-type (resting) animals registered in the subdataset (Mandino, et al., 2019). The data were previously preprocessed according to a common pipeline (https://github.com/grandjeanlab/MouseMRIPrep), and registered on the Allen volumetric atlas. In our analysis, we considered the activity in those voxels corresponding to the imported Allen connectome (Table 1). The empiric dataset did not distinguish between specific parts (e.g., ventral and dorsal) of certain brain regions (Anterior cingulate, Retrosplenial and Entorhinal areas). A unique time series was associated with each of these pairs of regions.

The empirical human EEG/fMRI dataset was acquired and preprocessed at Charité-Universitätsmedizin Berlin (Schirner et al., 2018) and made available in online repository (https://osf.io/mndt8/; Schirner, 2018). In summary, from a larger cohort (49 subjects, 18–80 years), 15 youngest subjects (18–31 years) were selected based on the quality of the EEG recording after correction of the MR artifacts. For each subject, diffusion-weighted MRI, T1-weighted MRI, and EEG-fMRI in resting-state paradigm were obtained. The T1-weighted image was used to parcellate the cortical gray matter into 68 regions according to the Desikan–Killiany atlas (Desikan et al., 2006). This definition of regions was then used to estimate the structural connectivity from the dw-MRI data (Schirner et al., 2015), and to extract the regional average time series from the fMRI data. The EEG data (Easy-cap; 64 channels, MR compatible) was treated with a high pass filter at 1.0 Hz followed with MRI acquisition artifact removal using Analyser 2.0 (v2.0.2.5859, Brain Products). The resulting sensor-level time series was downsampled to 200 Hz and low pass filtered to 30 Hz before correction for physiological artifacts (ballistocardiogram, muscle activity). Next, EEG source imaging was performed to obtain projected activity on the cortical surface and averaged within the 68 regions of the Desikan–Killiany parcellation. See Schirner et al. (2018) for a detailed description of both

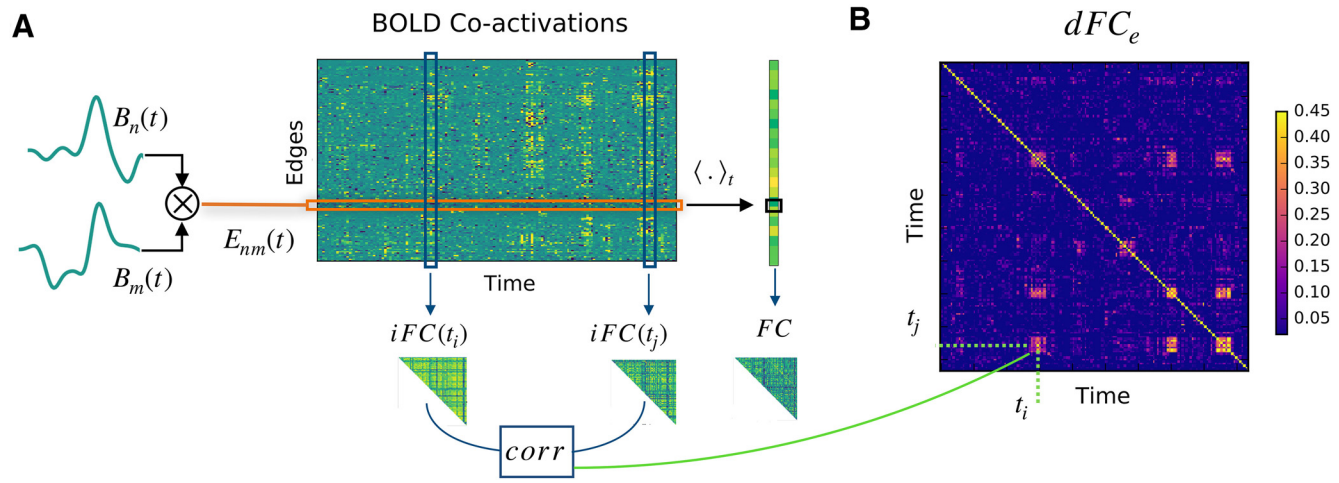

Figure 2. Two regimes of *dFC*. ***A***, Given two nodes *n* and *m* the edge CA signal $E_{nm}(t)$ (orange box) is defined as the product of the z-scored BOLD signal $B_n(t)$ and $B_m(t)$. Averaging the BOLD-CA matrix over time we obtain the Pearson correlation across each pair of brain regions *n* and *m* (in black box, right), defining the static *FC*. Each column of the BOLD-CA matrix represents an istantaneous realization of the *FC* (*iFC*). ***B***, The elements (t_i, t_j) of the dFC_e matrix are defined as the Pearson correlation between $iFC(t_i)$ and $iFC(t_j)$. Note in panel ***A*** the presence of transient bouts of strong BOLD-CA (e.g., in the blue boxes). During these events, the *iFC* remains relatively correlated for few consecutive time points, which gives rise to diagonal (yellow) blocks in the dFC_e matrix. The same CA burst (e.g., at t_i) can re-occur in time after long periods of time (e.g., at t_j), which gives rise to an off-diagonal dFC_e block (e.g., at the crossing of the dashed lines in panel ***B***).

fMRI and EEG processing. After the preprocessing, we made a quality check of every subject data and excluded BOLD points and associated EEG time windows [BOLD time repetition (TR) = 1.94 s = 388 EEG samples] which presented residual artifacts (at either EEG or fMRI level) based on the following criteria: if any of the six time series of the motion degrees of freedom (resulting from the FSL MCFLIRT head movement correction step) presented a peak; if the EEG window contained fluctuations simultaneously affecting most of the frequencies (time-frequency analysis); and if the EEG presented fluctuations above 7 SDs.

We finally selected 30 artifact-free trials of consecutive EEG/fMRI acquisition (minimum duration 2 min) across the cohort.

Time-dependent *FC*

To quantify the temporal evolution of the brain *FC*, we have employed two approaches: windowed *dFC* (dFC_w), and edge-*dFC* (dFC_e). Let us denote by $B_n(t)$ the regional BOLD time-series for each node $n = 1...N$. To compute the dFC_w (Allen et al., 2014), we first obtain the series of *FC* matrices *FC*(*w*) at each sliding window $w = 1...N_w$, defined as the correlation matrices for the segments $B_n(t)|_{t_w}^{t_w+\tau}$ (we fix the window size τ = 60 s and window step 2 s). Next, we correlate the vectorized upper triangular parts of the *FC*(*w*) matrices at different time windows to obtain the dFC_w matrix:

$$dFC_w(w_i, w_j) = corr\left[triu(FC(w_i), triu(FC(w_j))\right]. \quad (7)$$

On the other hand, the computation of the dFC_e starts with the z-scored BOLD time series B_n (subtract the mean and divide by the SD). The edge time series is then computed as element wise multiplication along time for each pair of regions $E_{nm}(t) = B_n(t) \cdot B_m(t)$ for $n,m = 1...N$ (see Fig. 2*A*). Next, for each pair of time points t_1, t_2, we compute the dFC_e matrix elements (Fig. 2*B*) as the correlation:

$$dFC_e(t_i, t_j) = corr(E_{nm}(t_i), E_{nm}(t_j)). \quad (8)$$

A main difference among the *dFC* variants lies in the scope of z-scoring of the time series B_n. In the case of dFC_e the *z* score z_n is computed from the whole time series, whereas in the dFC_w the *z* score is performed within the Pearson correlation in each time window $[t_w, t_w+\tau]$ separately.

Surrogate BOLD models

In order to compare our results below (Results, Neuronal cascades subtend RSN dynamic) about the origin of the *FC* dynamics with the null hypotheses of a random evolution and of inter-regional stationarity of the *FC*, we build time-shuffled and phase-randomized surrogates of the *FC* dynamics, respectively. The time-shuffled surrogate is obtained by randomizing the order of the instantaneous *FC*s *iFC*(*t*), i.e., the columns of the edge CA time series $E_{nm}(t)$ (see Fig. 2*A*). According to Hindriks et al. (2016) the phase randomized surrogate is obtained by adding a uniformly distributed random phase to each frequency of the Fourier transformed signal, and subsequently retrieving the phase randomized signals by anti-Fourier transform. Importantly, the phase shift is different at every time point but can be applied uniformly to all the brain regions (cross-spectrum preserved) or separately in every region (cross-spectrum not preserved). Only in the first case the bursts of CA are not destroyed but shifted (Extended Data Fig. 9-1*A*) and the static

FC is preserved. The coherent fluctuations around the stationary *FC*, however, are destroyed. For more details, see also Prichard and Theiler (1994).

Results

We start by introducing the synthetic setup used to simulate the main feature of *RSN* dynamics, i.e., the intermittent epochs of stable *FC*. To achieve recurrent functional network activation we set the brain regions into a bistable regime, where the mean membrane potentials can exhibit a resting (down) and a depolarized (up) state (Hansen et al., 2015). When the regions are suitably coupled over a connectome, the local activity spontaneously fluctuates between these states, which promotes system metastability, i.e., the recurrent exploration of multiple network configurations (Deco et al., 2017; Beim Graben et al., 2019). In order to understand the mechanisms allowing the dynamic coordination of bistable neural masses into multistable network re-configurations, we looked in detail at the building blocks of our simulation.

Rules of single and coupled nodes dynamics

Let us first consider the dynamics of a single isolated brain node (not connected to the network) where the local NMM parameters are tuned to ensure bistability. If there is no input current (I_{ext} = 0), solving the model equations (see Materials and Methods) resolves the dynamics of the node in terms of the mean firing rate $r(t)$ and mean membrane potential $V(t)$. The motion trajectories are represented on the (r, V) phase plane (Fig. 1*B*, left panel).

If, at a given time, a node takes a given (r^*, V^*) value, the direction of the arrow at these coordinates indicates the direction of the flow, and where the node dynamics will end up: either falling in the down stable state where the neurons populating the NMM exhibit low firing rate and strong (negative) membrane potential; or spiraling in a damped oscillation into the up stable state, in which the neurons display high average firing rate and low average membrane potential. Thus, in the absence of noise, neuronal activity of the node would rapidly freeze into a stable up or down level of activity (Fig. 1*B*, full dots).

Introducing noise allows the stochastic exploration of the phase space. If the noise is sufficiently large, a random movement in the phase plane can provoke the sudden switch from up→down or down→up basins of attraction (Fig. 1*B*, light blue and white shades, respectively), therefore changing the r and V dynamic modality.

We now consider a non-null input current I_{ext}, simulating a constant synaptic input. As I_{ext} increases (Fig. 1*B*), the two branches of the V-nullcline ($\dot{V} = 0$ lines) move horizontally away from each other, while the r-nullcline ($\dot{r} = 0$ line) remains fixed. Correspondingly, the location of the stable points in the phase plane shifts (at $\dot{V} = \dot{r} = 0$) and their basins of attraction change in size. The separatrix, i.e., the line separating the up and down basins of attraction, is therefore a dynamical element: its location depends on the amount of input that the node is receiving at a given time.

If I_{ext} is small, the separatrix is close to the up state (Fig. 1*B*, left) and the crossing of the separatrix via random fluctuations is more probable in the up → down direction; the node explores only the down state. Conversely, if the separatrix is close to the down state when I_{ext} is high (Fig. 1*B*, right), the node likely remains in the up state.

This property of the NMM is key to understand the system's dynamic. At a given time t the inputs received by node n will shift the separatrix, and make it easier (or not) for the node to change its activity as a function of noise and of its current state [(r^*, V^*) coordinates at time t].

Using this NMM, we simulate whole-brain dynamics in a mouse brain avatar (Melozzi et al., 2017, 2019), the detailed connectivity of which is imported from the tracer experiments of the Allen Institute and is parcellated into anatomic ROIs, associated with the network nodes (Fig. 1*C*; Oh et al., 2014). The communication between regions is weighted by the structural links W_{nm} of the structural connectivity (Fig. 1*D*). Thus, the input I_{ext} of a node represents the synaptic drive from the firing rates r_m of all the m nodes that are connected to node n (Fig. 1*E*; see Materials and Methods). As an effect of the coupling, the (projected) phase plane (r_n, V_n) at node n can be thought of as a distorted version of the phase plane of a single isolated node, where the location of the separatrix depends on the structural role that region n plays in the network hierarchy. Less connected regions receive a weak input current I_n so that the local phase plane is slightly distorted. Instead, regions with high centrality in the connectome, or that are part of strongly connected structural motifs, receive a strong input, which causes a greater distortion of the local phase plane, with consequences on their activity.

CA bursts account for *RSN* dynamics

Once a working regime is chosen by the selection of global and local model parameters, the raw outcome of the simulation consists of a high time-resolution neuroelectric signal: the average firing rate r and membrane potential V for each node. As a convention, we refer to the average firing rate activity as the simulated EEG data. With a further processing step, we obtain a low time-resolution simulated BOLD activity by filtering the membrane potentials through the Balloon–Windkessel model (Friston et al., 2000; Fig. 1*A*, right).

In order to compare simulated and empirical whole-brain imaging data, we analyze the dynamic evolution of functional brain patterns with *dFC* measures (Majeed et al., 2011; Smith et al., 2012; Hutchison et al., 2013; Lindquist et al., 2014; Karahanoğlu and Van De Ville, 2015; Shine et al., 2015). The most diffuse definition of *dFC*, is based on a sliding window approach (Allen et al., 2014). In brief, inside each time window, a static *FC* is computed as the correlation matrix of the BOLD activities. Then, the entries of the dFC_w matrix are defined as the correlation between the *FC*s at different windows (see Materials and Methods). In typical empiric datasets, dFC_w matrices show non-trivial block structures; diagonal block structures represent epochs of stable *FC*, while the off-diagonal blocks mark the re-occurrence of correlated *FC*

at distinct times. For our analysis, we introduce a *dFC* measure derived in an edge-centric approach, where the dynamics for the edge E_{nm} is defined by the product of the z-scored BOLD activities B_n and B_m at nodes *n* and *m* (Faskowitz et al., 2020). The resulting edge CA time series (Fig. 2*A*, orange box) tracks the temporal unfold of correlations across node pairs.

In fact, averaging the edge CAs across time defines the Pearson correlation across each pair *n* and *m* (Fig. 2*A*, right, black box). The correlation for each couple of regions (i.e., each edge) defines the static *FC* (Fig. 2*A*, right). Thus, we can interpret the columns in Figure 2*A*, blue boxes, as instantaneous realizations of the *FC* (*iFC*) at different times *t*. The dFC_e (Fig. 2*B*) is defined (without the use of sliding windows) by the Pearson correlation of the *iFC*s at each couple of times t_i and t_j. On the one hand, the window approach to *dFC* allows a more reliable measure of the correlations to the detriment of the resolution over the temporal structure. On the other hand, the edge approach is more sensitive to spurious correlations but, crucially for our following analysis, it maintains the full time resolution of the BOLD signals. Notably, the example Figure 2*A* extracted from a regime of interest, reveals that short duration bouts of strong BOLD-CAs (vertical stripes) spontaneously appear in association with a non-trivial dFC_e. As a final remark, we also notice that the dFC_e blocks (Fig. 2*B*) occur in coincidence with the strongest edge CAs, an observation that will have important consequences in our final analysis.

Multiple pathways to simulate *RSN* dynamics

To search for regimes of dynamic resting-state activity, we explore the parameter space by varying the global synaptic coupling *G* and the noise *N*, representing the impact of the structure over the local dynamics, and the stochastic currents simulating a generic environmental noise (thermodynamic, chemical, synaptic...), respectively. Then, we look for regions of the parameter space where a non-trivial functional network dynamics emerge. We define the "switching index," i.e., the variance across all elements of the upper triangular part of the dFC_w matrix (Fig. 3) to quantify the temporal irregularity of functional activity (roughly speaking, the number of different dFC_w block structures and how often they switch between one another). We identify two regimes giving rise to *RSN* dynamics, where the respective neuroelectric correlates are qualitatively different.

In the first case, a weak structural coupling (low *G*) is insufficient to promote any region into a high firing rate state, because the excitatory drive received by any node is relatively small. However, all regions can transiently reach a high firing rate state because the stochastic drive is strong. We refer to this as the monostable regime (Fig. 3, bottom left). In the second case, the stronger structural coupling pushes a subset of regions into a strongly active state leaving the remaining regions in the down state. A weak stochastic drive ensures stable dynamics with few regions jumping between the up and down states. We call this the bistable regime (Fig. 3, bottom right).

In conclusion, the balance between the local dynamics and the global connectivity (tuned by *G*), together with appropriate levels of perturbation of the system (*N*), allow the same NMM model to generate diverse large-scale organizations qualitatively similar to those measured empirically.

Before moving on, let us notice that the block structures in the dFC_w (examples in Fig. 3, bottom panels) give the impression that whole-brain dynamics is organized by a sequence of transient but long-lasting stable periods of correlated activity. However, the analysis of the corresponding dFC_e reveals that whole-brain dynamics is in fact characterized by much smaller periods of CAs. Since we want to compare resting-state dynamics to the underlying fast neuronal activity, we are interested in the highest temporal resolution available. Therefore, unless differently specified, in the following analysis we use dFC_e. We also notice that when dFC_w is used, as the window slides in time, it will capture the transient edge CA bursts as long as the latter is present in the window, giving rise to spurious long-lasting block structures (e.g., see the different block organization between dFC_w and dFC_e in Fig. 3, bottom right). Next, we analyze the neuronal mechanisms underlying resting-state functional dynamics generated by the model.

A generative mechanism for slow cascades of neuronal activations

Functional dynamics and the underlying neuronal activity fundamentally differ in their intrinsic time scales. Neuronal fluctuations typically evolve at the milliseconds scale. *RSN* dynamics unfolds in the order of tens of seconds. In this section, studying the results of our simulation, we reveal a potential mechanism by which local neuronal perturbations can generate a slow cascade of activation across the brain network, thus approaching the temporal scale of *RSN* dynamics.

To do so, we introduce a framework to interpret the simulated firing rate dynamics and its dependence on the structural connectome. We focus on the bistable regime where the low noise level allows a clearer visualization of the dynamic mechanisms in act. The hypotheses developed here will be later tested on the monostable regime as well as in empiric data. We identify five main categories of nodes based on their simulated firing rate activity:

- (D) down regions (Fig. 4*A*, light blue) display a low firing rate state throughout the duration of the simulation, as the up state is practically unreachable by noise-driven fluctuations. According to the section above, Rules of single and coupled nodes dynamics, the separatrix lies close to the up state (Fig. 4*B*, top). Their low firing rate regime (Fig. 4*B*, bottom) makes them poor communicators in the network hierarchy.
- (U) up regions (Fig. 4*A*, light red) always show a high firing rate (Fig. 4*B*, bottom), constantly providing inputs to their targets. The separatrix is close to the down state and is never reached (Fig. 4*B*, top).
- (J) jumping regions (Fig. 4*A*, green) undergo regular local transitions, dwelling for a relatively long time in both low-firing and high-firing rate states (Fig. 4*B*, bottom). In the projected phase space of these regions,

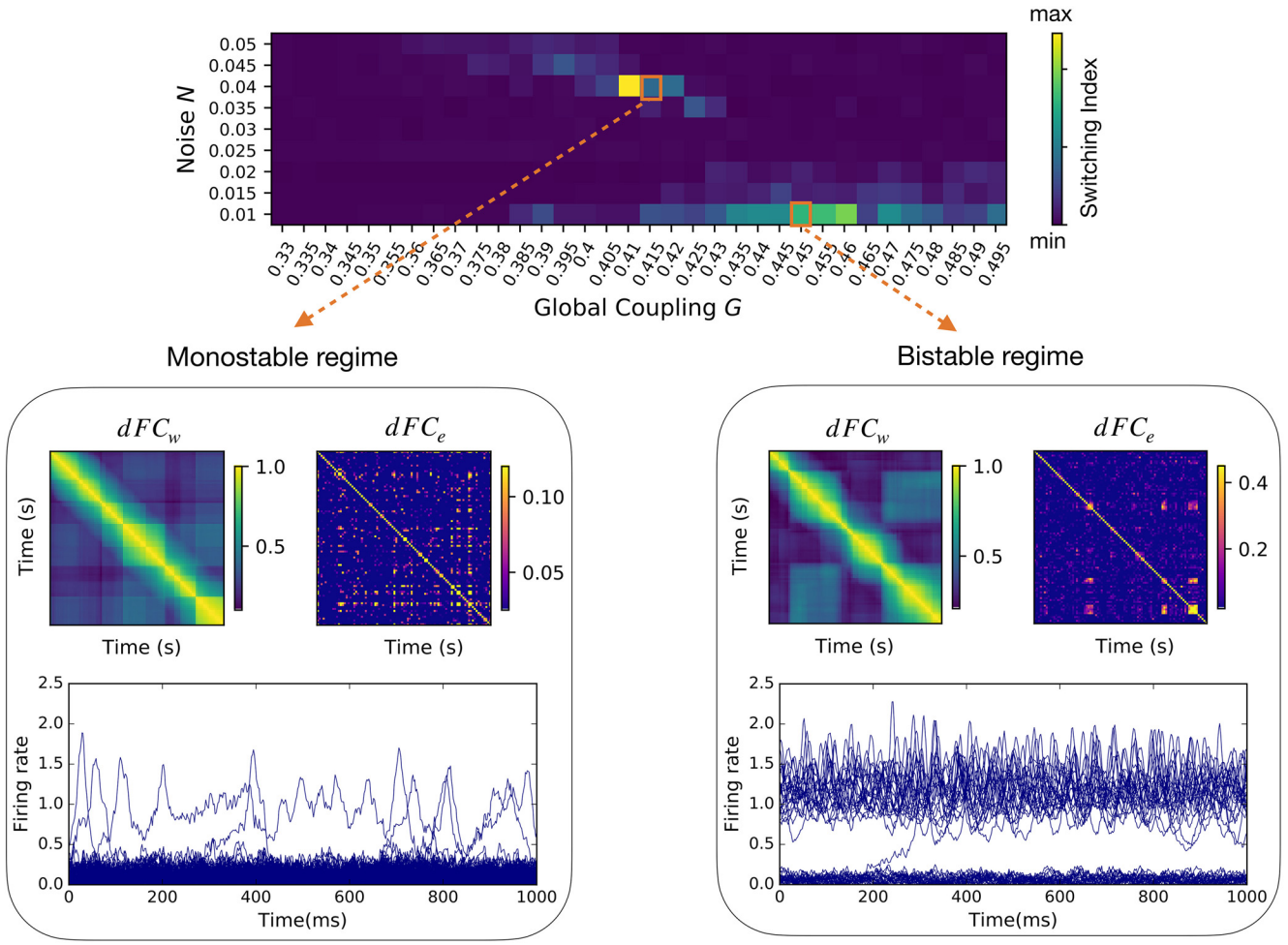

Figure 3. Two qualitatively distinct regimes of non-trivial functional dynamics. For every couple of global parameters (*G*, *N*) we calculated the *dFC* in a sliding window approach (dFC_w; as in Materials and Methods) and in an edge-centric approach (dFC_e; as in Fig. 2*A*,*B*). The "switching index" of each dFC_w matrix was evaluated as the variance of the respective upper triangular elements. We find two regimes of activity, named monostable and bistable, where qualitatively distinct neuroelectric organizations give rise to large-scale functional dynamics characterized by a non-vanishing switching index. In both regimes, the dFC_w and dFC_e display off-diagonal blocks, demonstrating a correlation between the functional activity at distinct times. The low global coupling *G* in the monostable regime (bottom left) does not guarantee a strong communication between the brain network regions, which most of the time populate the low firing rate ("down") state. A strong noise *N* pushes the brain regions in the high firing rate ("up") state for short transients. A higher value of the global coupling in the bistable regime (bottom right) promotes a subgroup of regions in the high firing rate (up) state. Low levels of noise perturb the equilibrium of the system provoking localized switching in both up →down and down →up directions (e.g., at $t = 200$ ms).

the separatrix lies midway between the up and down states (Fig. 4*B*, top). Therefore, they have the same probability to jump from up to down and vice versa Note that the timing of the (J) jumps defines a new slow time scale for the system. The fact that these jumps occur on a regular basis during the simulation ensures that this time scale is ever-present in the large-scale network dynamics.

- (D*) down-up regions (Fig. 4*A*, dark blue in network plot) have a stable activity around the down state fixed point but, in rare occasions, manage to reach the up state stable focus for a certain transient time.
- (U*) up-down regions (Fig. 4*A*, dark red in network plot) have a stable activity around the up state but are occasionally driven into a short-lived excursion to the down state.

The topographic organization of the firing rate classes shows the influence of the connectome in organizing whole-brain dynamics (Fig. 4*A*, regions labels in Table 1). Nodes receive different inputs as a function of the location in the connectome, which grants a different jumping probability and therefore a different role in network dynamics. A stochastic jump is a functionally important event for the network, as it corresponds to a sudden firing rate increase or decrease, which greatly influences the activity of downstream nodes. Thus, since the nodes of class (J) can jump regularly, we expect them to have a major role on whole-brain dynamics. A principal component analysis (PCA) of the regions' firing rates shows that nodes (J) are the main contributors to the first three principal components, explaining most of the system variance (explained variance ratio >0.59; see Extended Data Fig. 4-1*A*).

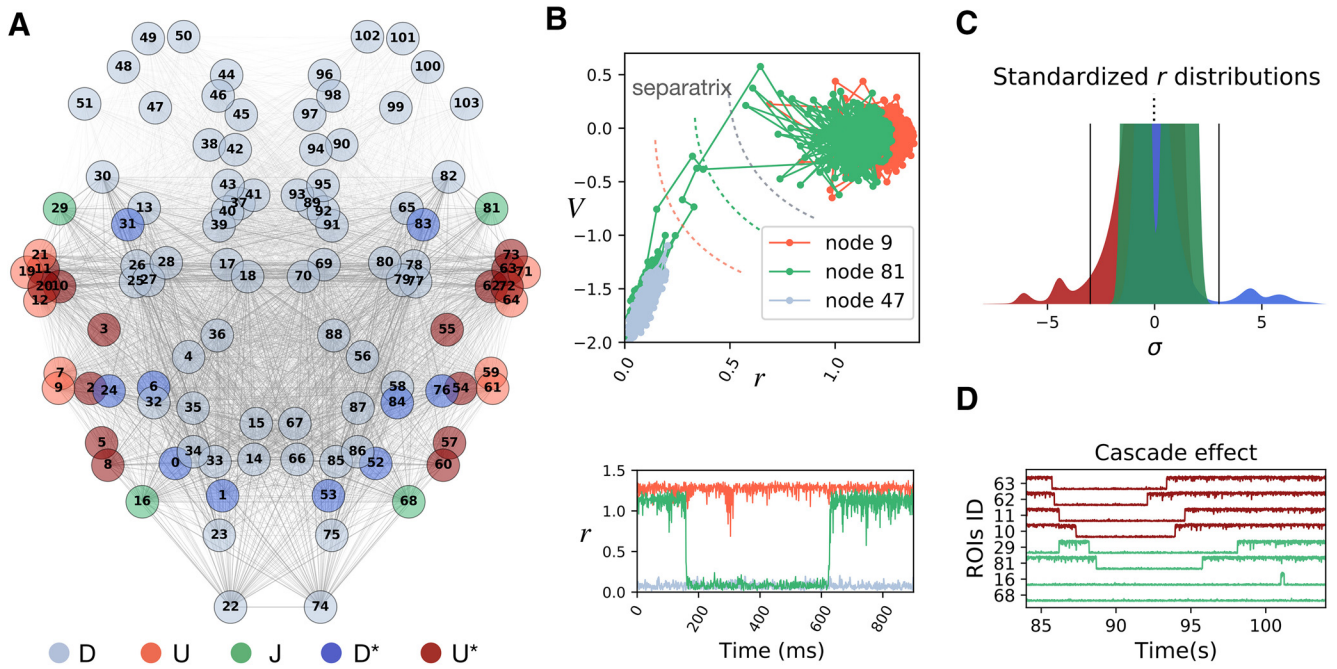

Figure 4. Mechanisms of cascade generation in the synthetic model. ***A***, Different regions have a different fate depending on their location in the connectome. We classified the regions in five classes (D, U, J, D*, U*) according to their activity. ***B***, Example exploration of the projected 2D phase space (top) and firing rates activity (bottom) of the "up-U" (light red), "down-D" (light blue), and "jumping-J" (green) regions. ***C***, Distribution of the standardized firing rates in different classes. Class (J) regions have two modes but never cross the $\pm 3\ \sigma$ threshold (black lines). Class (U*) (dark blue) and class (D*) (dark red) regions dwell most of the time in the up and down states, respectively. Only in important rare occasions the *-regions cross the threshold to jump on the other side, substantially deviating from their baseline activity. The leading role of the *-regions as compared with the other classes is shown using PCA in Extended Data Figure 4-1*A*,*B*. ***D***, Example of a cascade: when the (U*) node 63 jumps into the down state, it first drags down the node 62 (with which it shares the strongest structural link in the network). After them, other strongly connected nodes follow the trend.

Another key element of the simulated network dynamics is the occurrence of rare events, identified by large deviations, e.g., above 3 SDs σ away from baseline firing rate (Fig. 4*C*, black lines). Given their regular jumping, the activity of regions (J) never grows above 3 σ (Fig. 4*C* , bimodal distribution of standardized firing rate in green). The same holds for (D) and (U) regions. In contrast, we find that the regions in classes (D*) and (U*), occasionally grow above 3 σ during their rare jumps across the separatrix (Fig. 4*C*, dark blue and dark red distribution, respectively). Our simulation shows that these rare events can trigger cascades of transitions across the separatrix of a subset of regions (e.g., Fig. 4*D*). The propagation of a cascade depends on the structural location of the source node. Let us consider the case of a node with jumping potential, which is also a hub for the network (i.e., with high centrality; van den Heuvel and Sporns, 2013). Its local reshaping will have a wide influence throughout the network. However, the hubness of a jumping node does not guarantee the crossing of the separatrix by its target regions. If the hub is connected to a very stable subset of regions, following a jump of the hub, most of the separatrix lines in the targets will be slightly shifted, but not enough to allow any crossing. In contrast, if there exists a subset of strongly connected nodes with jumping potential, the jump of one will have strong effects within such subnetwork. In order to illustrate this point, let us consider that a group of nodes from class (U*), have very strong links binding them. Then, the occasional jump down of one of these nodes will strongly shift the separatrix of the other (U*) nodes toward the up stable focus, increasing their probability of jumping down. Then, many (U*) nodes will be dragged down one after the other, facilitating the next jumps, producing a cascade effect (as in Fig. 4*D*). During this event, the (J) nodes get also involved, interrupting for some time their regular control over the network. A windowed analysis of the first principal component of the firing rate activity shows that the nodes in the *-classes are driving the system during these rare events (Extended Data Fig. 4-1*B*).

The cascade effects quickly drag the system away from its standard state, establishing short epochs of increased deviations from baseline activity (the average firing rate in classes D* and/or U* deviates from baseline; Fig. 5*A*, top). In our simulation we mark four of these epochs (I, II, III, IV; Fig. 5*A*, bottom; Fig. 4*D* refers to Epoch I) which are separated by long periods of standard activity.

Summarizing, we have described how the jumps of the firing rate at local sites are extremely relevant for the unfolding of the neuronal activity throughout the brain, as they provoke the largest perturbations in the system. If jumps happen with a certain regularity, they will generate a slow time scale in the system. This slow rhythm in our

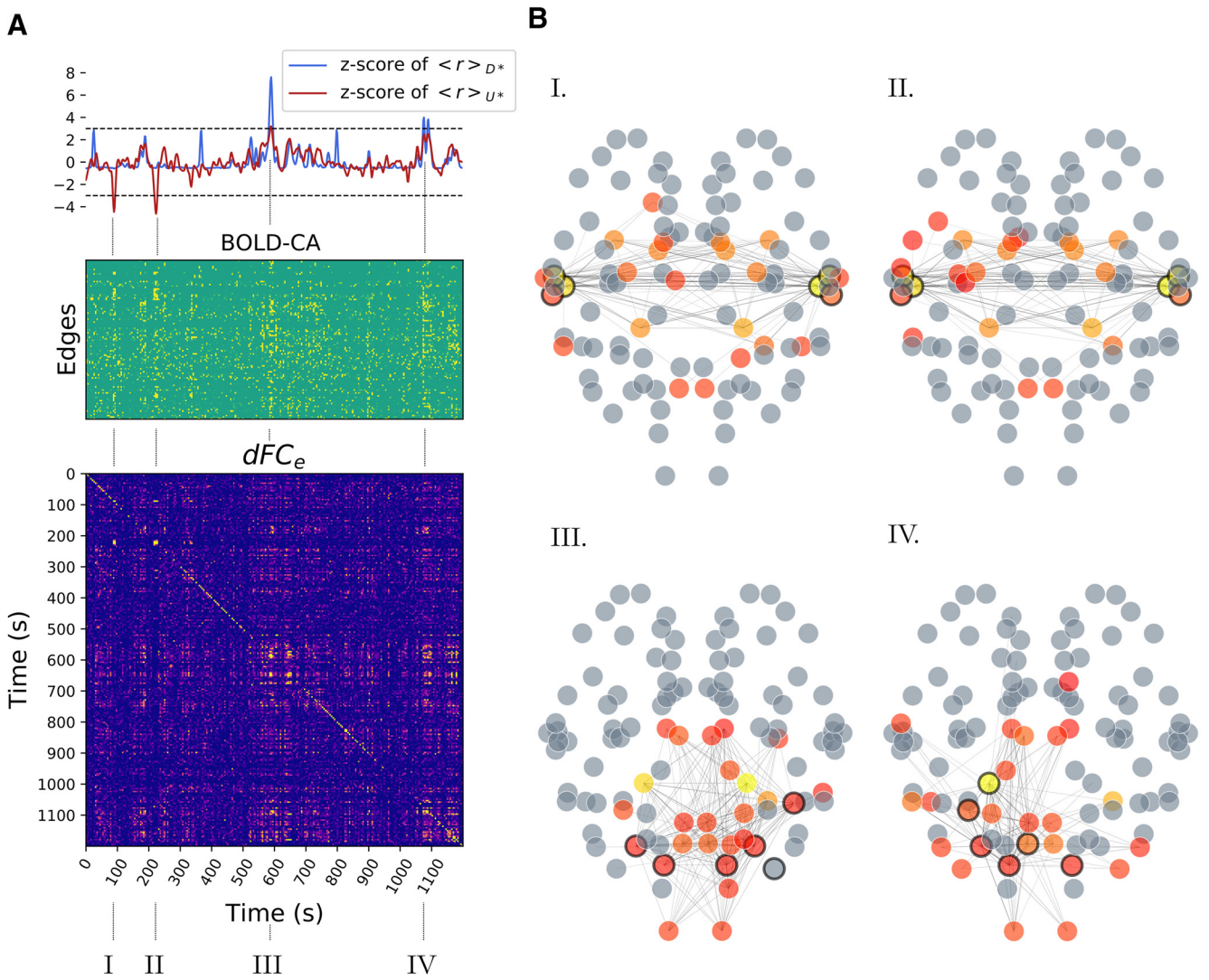

Figure 5. *RSN* formation. ***A***, top, The standardized firing rate activity in the (U*) and (D*) classes (class-specific average; dark red and dark blue, respectively) is characterized by peaks (the strongest are marked as I, II, III, IV) occurring in correspondence of cascades similar to Figure 4*D*. ***A***, middle, During a cascade, we also observe a peak of BOLD-CAs, appearing as vertical strips. Many, but not all, edges are recruited. ***A***, bottom, The blocks in the dFC_e matrix appear in correspondence of CA events, showing that these bursts generate stable epochs of *FC* correlated in time. ***B***, In each selected epoch (I, II and III, IV), the large firing rate cascades trigger the jump of other nodes away from baseline activity (circled in black) and promote specific functional hubs at the BOLD level, represented by colored nodes in the network plots. A functional hub is defined by the components of the first leading eigenvector (linear combination of brain regions explaining most of the variance in the data; eigenvalue $\lambda > 0.41$) associated to the *iFC*s at times t_I, t_{II}, t_{III}, and t_{IV}, respectively. The most representative hub regions are depicted in yellow. Gray regions have been excluded as they do not contribute substantially. Only the edges with the highest CAs are displayed. Importantly, CA events generated from neuronal cascades at specific sites support distinct functional networks which are not correlated among themselves (e.g., no off-diagonal dFC_e block between I and III).

simulations can be traced back to a small subset of regions (J) which transit between the up and the down states. These regions lead the baseline evolution of the entire system, acting as homeostatic agents which keep the system dynamics stable. On rare but important occasions this control weakens, which allows the propagation of a large cascade of activity. Such cascade effect takes place when a sudden local transition brings a typically stable region [(U*) or (D*)] away from baseline activity and induces other regions to reorganize. The cascade goes on until the noise and the structural pressure take the system back to its normal evolution, e.g., through the normalizing action of the jumping regions (J). We then explore whether such rare deviations from baseline activity account for resting-state brain dynamics.

Neuronal cascades activate distinct RSN

The previous analysis focused on the simulated (high time resolution) neuronal activity. We now look at the simulated (low time resolution) BOLD, which signals are characterized by collective CA (Fig. 5*A*, middle). Interestingly, these events are aligned to the large deviations from baseline of the firing

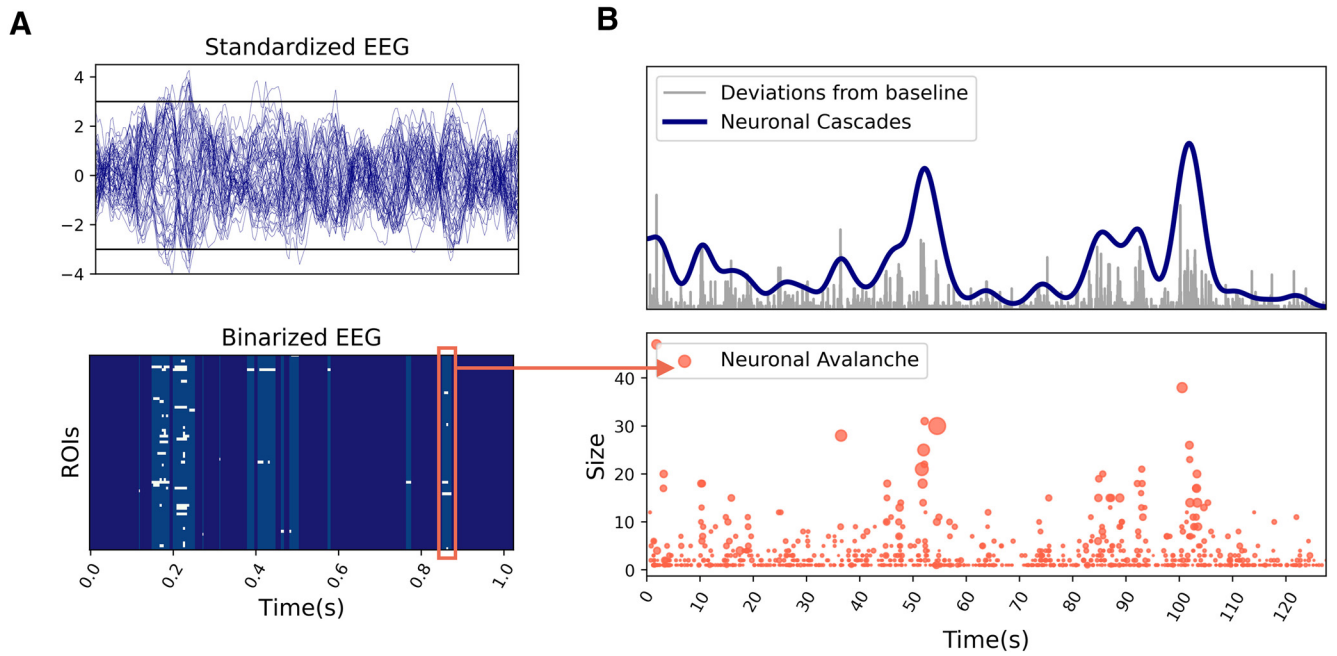

Figure 6. Neuronal cascades and neuronal avalanches. ***A***, Standardized EEG activity extracted from a resting-state human EEG/fMRI dataset (top). The activity is binarized assigning a unitary/null value every time the activity in a region is above/below a certain threshold (e.g., $\pm 3\ \sigma$; black lines). The obtained binary raster plot (bottom) is characterized by intermittent epochs of deviations from baseline activity. Neuronal avalanches are defined as consecutive deviations from baseline activity (e.g., red box). ***B***, We extract the global magnitude of the deviations from baseline (top, gray signal) by summing the binary EEG raster plot over the ROIs. This signal is convoluted with a Gaussian kernel [width = 1 BOLD TR] and downsampled to obtain the same resolution of the BOLD activity, which defines the neuronal cascades signal (blue). Neuronal cascades can be thought of as clustering of high magnitude avalanches, whose occurrence in time is not homogeneous (bottom).

rate activity of the (U*) class or the (D*) regions (Fig. 5*A*, top, Segments I, II and III, IV, respectively). When looking at the corresponding dFC_e matrix (Fig. 5*A*, bottom), we also note that the most stable dFC_e blocks correspond to the largest BOLD-CA events. This observation is not a triviality, since a higher CA does not imply a stronger correlation. The presence of off-diagonal blocks in the dFC_e shows that CA patterns are correlated when generated either by the (U*) or in the (D*) regions. In this example, the CA patterns generated by the jumps of distinct classes are not correlated. Each CA pattern defines the upper triangular part of an *iFC* (as in Fig. 2*A*). Figure 5*B* displays, for each selected epoch, the edges with the highest CA values. The functional hubs, a subset of regions with a central role in the functional dynamics, are defined in each epoch by the *iFC*'s leading eigenvector (Melozzi et al., 2017), and represented as different colors in the brain network plots (from red to yellow in a scale of importance). We highlight with a black rim the nodes whose firing rate deviated from baseline activity above a threshold (fixed at 3 σ). Notice that while the cascade generates at certain network locations (black rims), the dynamics of the RSN establishes a new emergent phenomenon at the large scale (colored nodes). The same perturbation can re-occur spontaneously eliciting similar functional networks correlated at distinct times, as it is marked by the off-diagonal blocks of the dFC_e (Network Plots I, II or III, IV). Summarizing, neuronal perturbations starting at different locations in the connectome elicit different BOLD-CA events, which result in distinct functional networks.

Neuronal cascades and BOLD-CAs in empiric data

In the previous sections, we described how the large spontaneous deviations from baseline activity play a key role in the simulated system dynamics by activating specific large-scale functional networks. Here, we hypothesize that a qualitatively similar network behavior takes place in empiric resting-state data (see Discussion). To test this, we provide a working definition of neuronal cascades as a global measure of such long-lasting perturbations of the neuroelectric activity (see Discussion). For illustrating the pipeline, we use an example trial from an EEG/fMRI resting-state human dataset (see Materials and Methods). First, we binarize the firing rate activity in every brain region by assigning a unitary value when its activity exceeds $\pm 3\ \sigma$ (Fig. 6*A*). Then, we define the magnitude of the deviations from baseline by summing the binarized EEG over the regions (Fig. 6*B*, top, gray line). Finally, we convolve the obtained signal with a Gaussian kernel (width = 1.94 s = BOLD TR) and we downsample it to the same time resolution of the BOLD signals to allow comparison. The resulting neuronal cascade signal (Fig. 6*B*, top, blue line) is characterized by bumps which describe a long-lasting increase in the magnitude of non-standard perturbations (e.g., above 3 σ). Neuronal cascades should not be confused with the concept of neuronal avalanches (Beggs and Plenz, 2003), which consist of consecutive deviations from baseline activity of a subset of brain regions or localized neuronal groups (Fig. 6*A*, bottom, example of a neuronal avalanche in the red box). The number of regions in the subset defines the size of

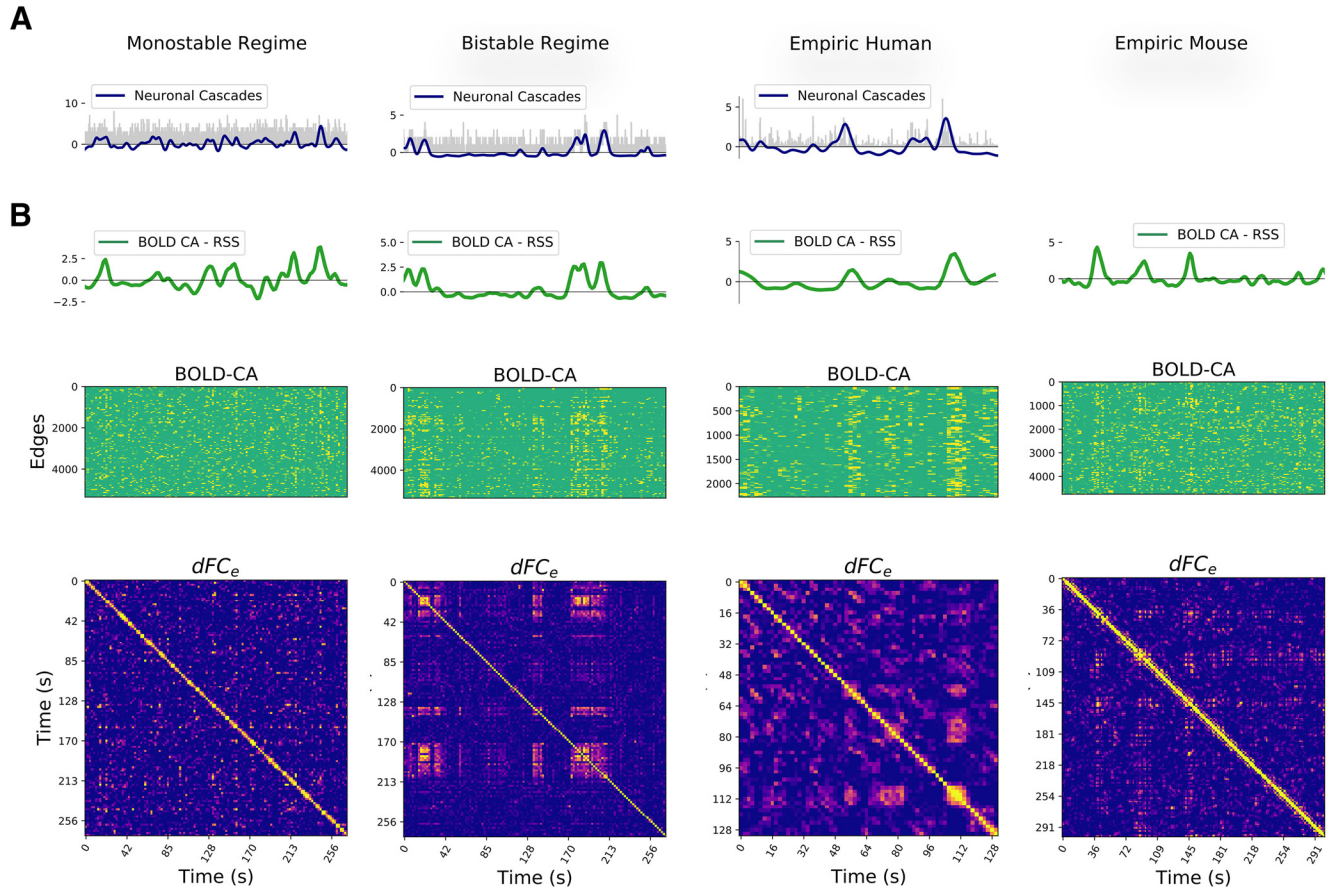

Figure 7. Neuronal cascades drive the functional dynamics. ***A***, Example of neuronal cascades in the monostable and bistable synthetic regime and for a representative subject of the empiric EEG/fMRI human dataset. ***B***, The BOLD-CA in simulated and empiric mouse and human datasets (middle panels) are characterized by sudden collective events involving large network parts (vertical stripes). The root sum square of BOLD-CA across all edges (RSS, green lines, top panels) defines the global CA amplitude signal for each dataset. Concurrently, the dFC_e matrices (bottom panels) display both diagonal and off-diagonal blocks, remarking the non-trivial re-occurrence of the same stable functional network at distinct times (see Fig. 2*B*). At a visual inspection, the BOLD-CA events happen in coincidence with dFC_e blocks and, most notably, the neuronal cascades and RSS signals (blue and green lines in panels ***B***, ***C***, respectively) co-fluctuate in most instances.

an avalanche, while the duration of the consecutive activations defines its lifetime (up to few hundreds of milliseconds in empiric data). Neuronal cascades are a global measure that describes a slower process on the order of tens of seconds. In Figure 6*B*, bottom panel, each red dot marks the occurrence of an avalanche of a certain size (dot size represents the duration). Remarkably, neuronal avalanches accumulate in correspondence with the largest neuronal cascades. Thus, we can think of the neuronal cascades as the clustering of neuronal avalanches. This first major result proves that the probability of observing strong brain fluctuations (including neuronal avalanches) is not constant in time, but increases during neuronal cascade peaks, which occur at an infra-slow time scale. Also, our simulation shows localized increases in cascade activity, which are shorter in the noisy monostable regime and more prolonged in the bistable regime (Fig. 7*A*).

At the level of fMRI, another *in silico* prediction is the presence of strong BOLD-CA events and their co-occurrence in coincidence with off-diagonal dFC_e blocks. We verify the presence of BOLD-CA events in synthetic, empiric mouse fMRI and in human EEG/fMRI datasets (Fig. 7*B*, central panels), suggesting that temporally inhomogeneous bursts constitute a generic dynamic modality of real(istic) brain networks. To show the relation with dFC_e, we first extract from the BOLD-CA signals the root sum squared (RSS) time series, which quantifies the amplitude of all edge CAs at each time point (Fig. 7*B*, green lines, top panels). Then, we partition the RSS signal in CA events and nCA non-events (respectively above and below the 98th percentile of the RSS values). We show that the correlation between any two events is statistically higher than the correlation between events and non-events as well as between couples of non-events (Fig. 8*A*). The results hold for synthetic and empiric results, which were pooled over several experimental trials. Since the correlation between CA patterns at different times correspond to the off-diagonal elements of the dFC_e matrix (as shown in Fig. 2*A*,*B*), we conclude that bursts of BOLD-CA events account for the highest off-diagonal values in the dFC_e in experimental datasets, as predicted by the model. In Figure 8*B*, we show an example of empiric human dFC_e

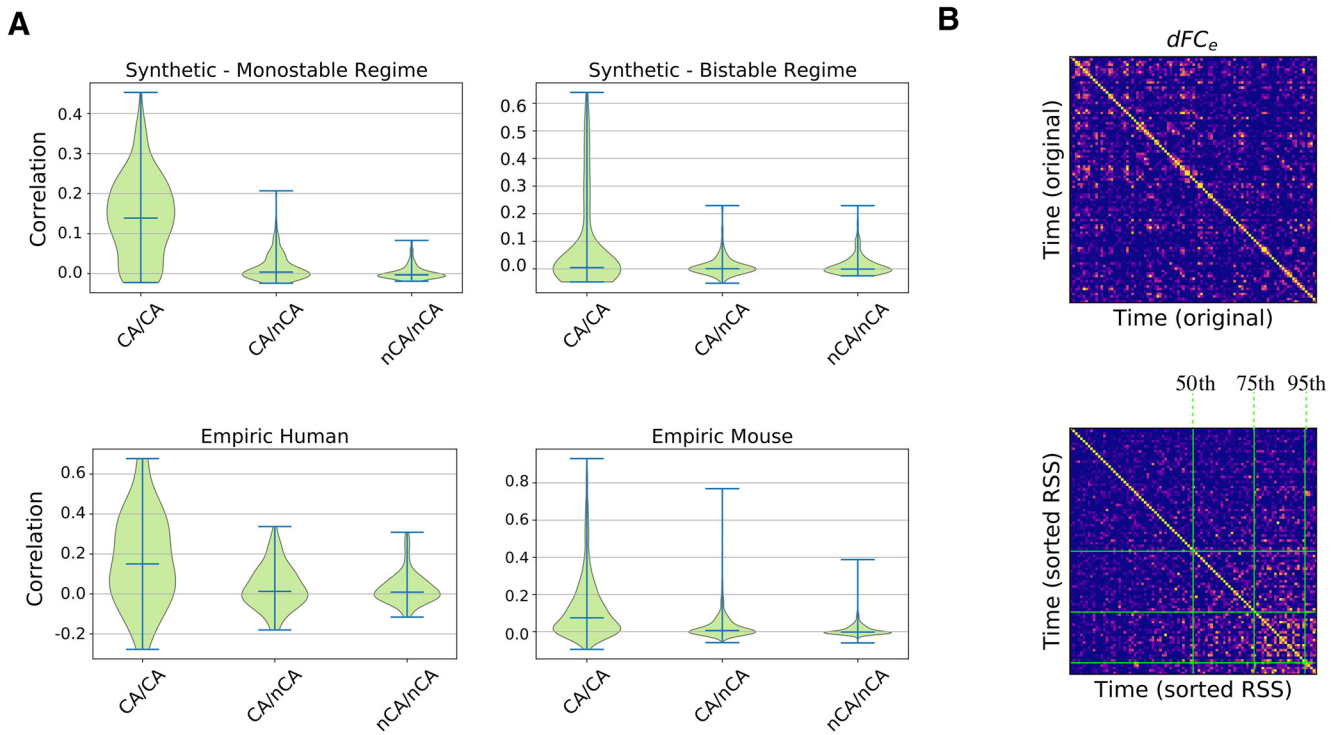

Figure 8. ***A***, The largest BOLD-CAs events (CA, above the 98th percentile of the RSS; Fig. 4*C*, green line) are distinguished from non-events (nCA, below threshold). We report the synthetic and empiric correlations between *iFC*s at times within CA events (left in every panel), between CA events and non-events nCA (center of panels), within non-events nCA (right of panels). These correlations are by definition the off-diagonal values of the dFC_e matrix (see Fig. 2*A*,*B*). The distribution of the correlations within events is wider and explains the greatest off-diagonal correlation values of the dFC_e across all the synthetic and empiric datasets. This principle is explicitly shown in panel ***B***, where the original dFC_e extracted from an empiric human trial (top) was sorted according to increasing RSS (bottom), leading to the clustering of high correlations toward high CA times. This shows that most of the non-trivial temporal correlations involve CA times falling in the last quartile of the RSS (above the 75th percentile, central green line). Thus, the strongest CA events drive the dynamics of *FC*.

(top), and the same matrix where times are sorted accordingly to increasing RSS. Green lines represent different percentiles (50th, 75th, and 95th) of the RSS. Notice that, in line with the results above, the non-trivial temporal correlations (yellow off-diagonal dFC_e elements) involve those time frames with the highest network CAs.

Neuronal cascades subtend RSN dynamics

Based on the theoretical results of the previous sections (summarized in Fig. 5), neuronal cascades should give rise to BOLD-CAs. In fact, a visual inspection of simulated and empiric data suggests the co-occurrence of neuronal cascades (blue lines in Fig. 7*A*) and BOLD-CA (RSS; Fig. 7*B*, green lines). Remarkably, a similar correspondence is present in an EEG/fMRI resting-state human dataset (best trial shown in Fig. 7), all the more since the simulations are done using a mouse connectome. To characterize this correspondence, we correlate the cascades signal with the BOLD-CAs amplitude profile. In both the monostable and the bistable regimes, the two measures are significantly correlated ($\rho \sim 0.54$ and $\rho \sim 0.91$, respectively). In Figure 9*A*, top, we report the correlations between the cascades and the BOLD-CA amplitudes across several trials of a human cohort (see Materials and Methods for trial selection). The correlation is conducted by shifting the RSS time series of a given time-lag. A peak of correlation appears naturally between the two measures when the BOLD signal is shifted backwards by two time points (3.88 s; Fig. 9*A*, bottom, blue line). Therefore, as expected, the EEG neuronal cascade signal precedes the BOLD-CAs by a few seconds. Notice that, in general, a shift forward of the BOLD activity results in a rapid loss of correlation.

Finally, to prove the statistical significance of our observations, we build surrogate BOLD signals and we compare the associated CA amplitudes to the neuronal cascade signal in each trial. In particular, we compare the observed cross-correlation profile (Fig. 9*A*, bottom, blue line) with the profiles extracted by correlation of neuronal cascades and surrogate CA amplitudes of three kinds: time-shuffled (example of cross-correlation profile in Fig. 9*A*, green line), phase-randomized, cross-spectrum preserved (example in Fig. 9*A*, orange line), and phase-randomized, cross-spectrum not preserved (example in Fig. 9*A*, purple line).

In all the surrogates, the functional dynamics is disrupted (see Materials and Methods). In the first two models, the static FC is preserved but its dynamic evolution is made trivial. Namely, the time-shuffled model consists of random *FC* jumps around a fixed pattern, while in the

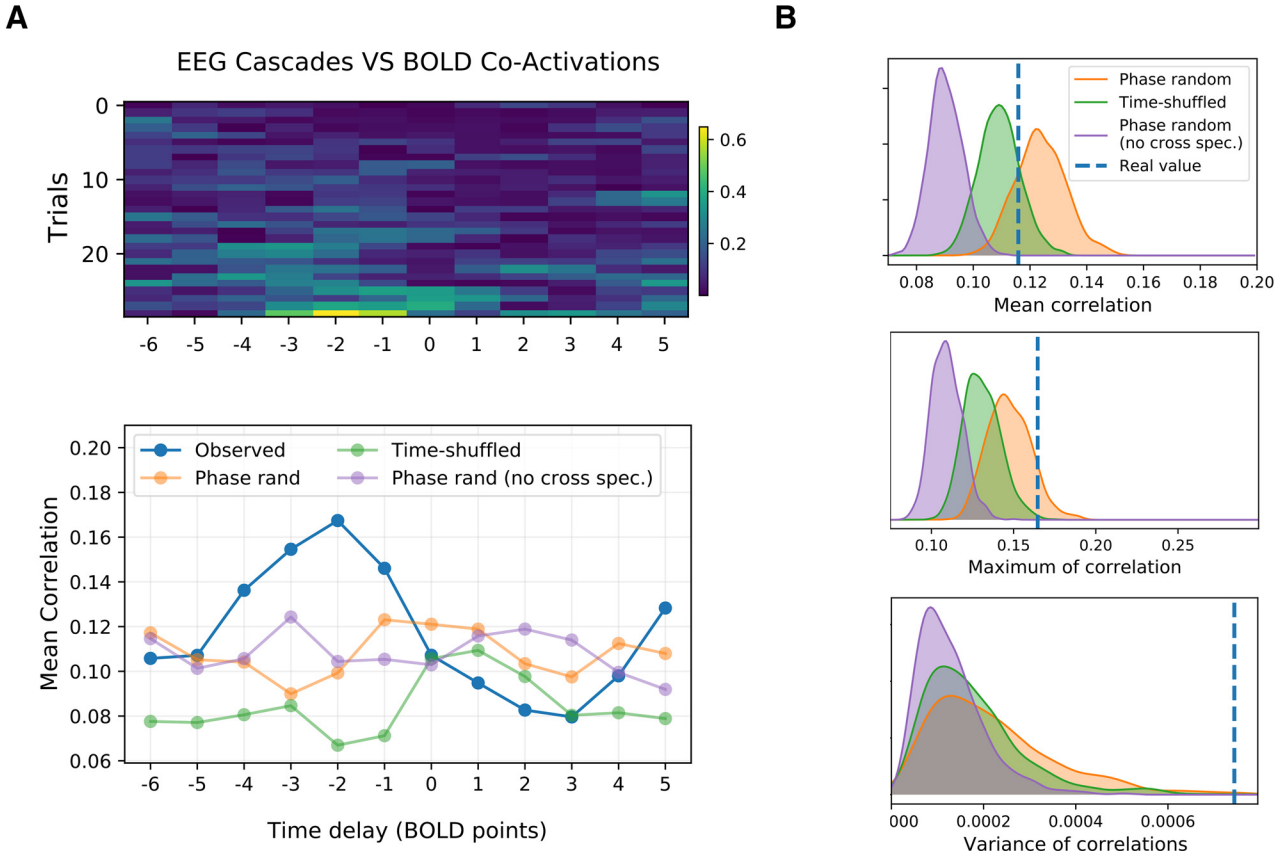

Figure 9. ***A***, top, Correlation between the cascade magnitude and the BOLD-CA amplitude (Fig. 4*B*,*C*, blue and green lines) for different time lags in several EEG/fMRI trials extracted from a Human cohort of resting subjects. Negative lag is associated with a shift backward of the BOLD signal. ***A***, bottom, The cross-correlation averaged across trials shows a clear trend (blue line). The peak of correlation at lag –2 sampling points (1 pt = 1.94 s), as well as the rapid fall for positive lags, confirms that the EEG precedes the BOLD activity by few seconds. The same profile is evaluated by comparing the largest cascades with the BOLD-CA signals extracted from 1000 time-shuffled (example in green), 1000 phase-randomized (cross-spectrum preserved, example in orange), and 1000 phase-randomized (cross-spectrum not preserved, example in red) BOLD surrogates for every subject (see Extended Data Fig. 9-1*A*,*B* for surrogate properties). ***B***, The distribution of the mean, maximum, and variance of the cross-correlations for each surrogate model is displayed and compared with the empiric values. In particular, the variance plot shows a clear significance of the results (single subject results in Extended Data Fig. 9-1*C*).

phase surrogate (cross-spectrum preserved), stationarity is strictly imposed by destroying any coherent fluctuation around the static *FC*. In fact, the latter corresponds to preserving the static correlations across node pairs, i.e., the average of the edge CA signals. These two surrogates also preserve the original fat-tail distribution of the BOLD-CA amplitudes (RSS values), and therefore supports bursty CA events (Extended Data Fig. 9-1*A*,*B*). When the cross-spectrum is not preserved, the static FC is corrupted and the CA amplitude distribution is normalized. For each surrogate type, we compute 1000 cross-correlation profiles. The distribution of their mean, maximum, and variance (averaged across all the trials) is shown in Figure 9*B*. The observed values are always significant when compared with the Phase-randomized surrogate with cross-spectrum not preserved. The observed mean values lie between the random (time-shuffled) and the ordered (phase-randomized) scenario (Battaglia et al., 2020). Only the Phase-randomized surrogate, where the cross-spectrum is preserved, reaches the peaks of correlation of the observed data, and the significance of the observed maximum is $p = 0.108$. The variance of the correlation profile is always significant ($p < 0.001$) as compared with all the surrogate models. The result holds in several instances at the single-subject level (Extended Data Fig. 9-1*C*). We conclude that neuronal cascades drive BOLD-CAs dynamics thus shaping whole brain resting-state *FC*.

Discussion

Cognitive function requires the coordination of neural activity across many scales, from neurons and circuits to large-scale networks (see Betzel and Bassett, 2017, and references within). As such, it is unlikely that an explanatory framework focused on any single scale will yield a comprehensive theory of brain activity, cognitive function or brain disease. Fast time scales evolve within the quasi-stationary constraints imposed by slow time scales. As the latter changes, the organization of the former must change consequently. Similarly, local neuronal events can

trigger large-scale complex responses (Houweling and Brecht, 2008; Huber et al., 2008). We demonstrated this principle along the organization of the fast neuroelectric correlates of the slowly evolving large-scale *dFC* patterns for two mammalian species. Large neuronal cascades, defined by collective deviations of the simulated EEG signals away from baseline activity, can emerge as BOLD-CA events, i.e., strong simultaneous fluctuations at pairs of regions across the brain network. In turn, the intermittent set of BOLD-CA events underlies specific stable *FC* epochs. Thus, we suggest that large neuronal cascades have an organizational role in the resting-state brain dynamics.

In this work, we have adopted a theory-driven approach to reproduce qualitatively the resting state *FC*, analyze its dynamics and trace it back to its neuronal correlates. The NMM used to simulate regional dynamics maps the activity of an infinite number of all-to-all coupled neurons, each described by a simple phase-oscillator equation, into the mean-field firing rate and membrane potential variables (Montbrió et al., 2015). Although not giving full access to biophysical processes, as when using detailed single neuron models, the model we used preserves important information about the microscopic neural network organization of a simulated brain region (e.g., the neuronal synchrony; see Materials and Methods). The low computational load enables the simulation of fMRI-like sessions in TVB. Our results prove that *FC* fluctuations can be self-generated on a connectome by random sudden changes in the local neural network organization. In our setup, the analysis of more spatially fine grained neural dynamics, e.g., in the form of cell assemblies Buzsáki (2010), is not accessible. Future applications allow the possibility of including synaptic dynamics (Taher et al., 2020), adaptation (Gast et al., 2020), excitatory versus inhibitory populations (Montbrió et al., 2015; Laing, 2017; Dumont and Gutkin, 2019), among others. The use of these models establishes a new venue to address multiscale phenomena, maintaining, to a certain extent, the co-existence of microscopic and macroscopic scales of organization (Coombes and Byrne, 2019).

To simulate the spontaneous emergence of dynamic functional networks we tuned each neuronal population into a bistable regime. We expect similar results to hold for other models supporting local bistability. In our case, we can directly interpret the two stable states as two configurations of the spiking neural networks. Varying the global couplings, we discovered two regions of the parameter space, defining the monostable and the bistable regimes, where the large-scale organization is dynamical, but qualitatively different. In both regimes, the neuronal activity is characterized by up and down states, which occurrence was observed both *in vitro* (Plenz and Kitai, 1998; Cossart et al., 2003) and *in vivo* under several conditions such as anesthesia, slow-wave sleep, quiet waking and also during perceptual task across several species (Steriade et al., 1993; Luczak et al., 2007; Vyazovskiy et al., 2011; Engel et al., 2016; Jercog et al., 2017). The functional dynamics in the two regimes also differs, e.g., in terms of the statistical properties of the BOLD-CA events (Fig. 8*A*) or in the life-time of the stable *FC* states (i.e., the size of the *dFC* blocks in Fig. 7*B*, bottom).

The generation of a variety of dynamic regimes from changes in the global "environmental" parameters is in keeping with the degeneracy principle, according to which multiple models and/or parameter settings capture the neuronal variability (Marder and Taylor, 2011), and it is expected also in biological systems. For example, sleep deprivation, which alters brain and body function (Medic et al., 2017), is associated with changes in the speed of the *FC* evolution (Lombardo et al., 2020). Accordingly, distinct features of the *dFC* should correspond to a different underlying neuroelectric organization (and perhaps to distinct mechanisms of communication across brain regions; Battaglia and Brovelli, 2020). The transition between wakefulness and sleep brain states offers an example of sudden change of the whole-brain dynamics associated with the microscopic neuroelectric re-organization (Larson-Prior et al., 2009; Boly et al., 2012; Tagliazucchi et al., 2016; El-Baba et al., 2019).

While the debate over the actual nature of *FC* dynamics is still ongoing (Hindriks et al., 2016; Laumann et al., 2017; Liégeois et al., 2017), several evidences were provided in favor of the *dFC* as a legitimate measure of the functional evolution (Preti et al., 2017). Here, we found that a large part of the functional information is condensed in large BOLD-CA events, in keeping with previous results (Zamani Esfahlani et al., 2020; see Fig. 5*A*). The occurrence of the BOLD-CA events cannot be ascribed to the spectral properties of the BOLD signals nor to motion artifacts (Zamani Esfahlani et al., 2020), which supports a genuine phenomenon. Our results provide an *in silico* support to a burst-based system dynamics where correlated CA events subtending RSNs occur intermittently and are separated by long low-activity periods. These results are in accordance with previous works showing that the relevant information about the major RSNs is carried by the largest fluctuations of the fMRI BOLD signals (Tagliazucchi et al., 2012a; Liu and Duyn, 2013; Allan et al., 2015; Cifre et al., 2017; Gutierrez-Barragan et al., 2019). The spontaneous bursts of BOLD-CA highlight recurring sets of network edges, which subtend special RSNs. How the system is organized around these preferential sets and what triggers the sudden co-fluctuations remain to be determined. Our analysis remarks the central role of the structural connectivity in this process, in line with a recent work suggesting that CA are shaped by structural modules (Pope et al., 2021). Here, we suggest that large neuronal cascades generated by sudden neuronal re-organization in source regions may play a central role in driving the exploration of the connectome and in determining the large-scale *FC* dynamics.

During the BOLD-CA events, the evolution of the *FC* slows down, as shown by the high correlation between functional states at consecutive times (Fig. 7*B*, bottom panels). An emergent stable *FC* elicited by a BOLD-CA event can persist for several seconds. The same state can re-appear after a few minutes in coincidence with another CA. In many dynamical systems, slowdowns and large-scale events are typically observed at the transition

between different states (or phases), i.e., at the critical point (Scheffer et al., 2009). Critical dynamic systems are characterized by other typical properties, including the presence of fluctuations at all spatiotemporal scales (Cocchi et al., 2017). Historically, the hallmark of a critical organization of the brain activity came from the observation of neuronal avalanches whose size and duration fit a power-law (Beggs and Plenz, 2003; for a "critical" look at brain criticality see Beggs and Timme, 2012).

In order to compare the fast EEG and the slower BOLD signals, we focused on the slow unfolding of the EEG deviations from baseline activity. In other words, instead of focusing on the size and duration of the neuronal avalanches, we analyzed their collective occurrence at the resolution of seconds, which we refer to as neuronal cascades (Fig. 6). We showed that the cascade magnitude is correlated to the BOLD-CA amplitude (Fig. 9*A*). In particular, in the empiric human dataset we observe a rapid drop of this correlation when the BOLD activity is shifted backward with respect to the EEG signal. This fact makes our result more robust since we expect a change of the BOLD activity to happen after a sustained neuroelectric activity.

Notice that in the empiric data set, not all the neuronal cascades give rise to BOLD-CAs, and not all the BOLD-CAs are preceded by large neuronal cascades. In general, we should expect a non-trivial interaction between these phenomena and other infraslow processes. For example, a growing corpus of evidence relates the slow functional and neuroelectric dynamics with other physiological and cognitive infraslow processes such as neuromodulation (Shine et al., 2016), visceral (heart and gut) inputs (Azzalini et al., 2019), and cognitive performance (Monto et al., 2008).

In the cases in which neuronal cascades and BOLD-CA events co-occur, we can hypothesize that the stable *FC* state evoked by a CA event is related to the specific structural channels in which the neuronal cascade spreads. In fact, we showed in the simulated data that the largest neuronal cascades underlie specific functional patterns (Fig. 5), depending on the location of the onset. Also, the observation that the same cascade appears at regular intervals (see for example the three peaks at second ~100, ~200, and ~300 in Fig. 5*A*) suggests that the re-occurrence of the same stable patterns in time can be traced back to the increased probability of the same cascade to occur following a first large event, in the same way an after-shock follows the main earthquake. It is interesting to note that, as in our model, correlated bursty events associated with memory effects are observed in many natural systems (Karsai et al., 2012).

The above hypotheses require further exploration of larger empirical datasets. In the model, we have shown that the multiscale mechanistic origin of large cascades can be understood ultimately by the interplay between the local neuronal organization, the stochastic nature of its sudden re-organization and the structural constraints it obeys. The present work provides a new understanding of whole-brain functional dynamics, which is shaped by neuronal cascades giving rise to large BOLD-CA. Since most neurologic disorders are characterized by complex reorganizations at the neuronal scale, it will be interesting to determine whether specific alterations in neuronal cascades sign specific neurologic disorders, and explain the already identified alterations in whole-brain dynamics.

References

Allan TW, Francis ST, Caballero-Gaudes C, Morris PG, Liddle EB, Liddle PF, Brookes MJ, Gowland PA (2015) Functional connectivity in MRI is driven by spontaneous BOLD events. PLoS One 10: e0124577.

Allen EA, Damaraju E, Plis SM, Erhardt EB, Eichele T, Calhoun VD (2014) Tracking whole-brain connectivity dynamics in the resting state. Cereb Cortex 24:663–676.

Azzalini D, Rebollo I, Tallon-Baudry C (2019) Visceral signals shape brain dynamics and cognition. Trends Cogn Sci 23:488–509.

Battaglia D, Brovelli A (2020) Functional connectivity and neuronal dynamics: insights from computational methods. In: The cognitive neurosciences (David Poeppel GRM, Gazzaniga MS, eds). Available at https://hal.archives-ouvertes.fr/hal-02304918.

Battaglia D, Boudou T, Hansen ECA, Lombardo D, Chettouf S, Daffertshofer A, McIntosh AR, Zimmermann J, Ritter P, Jirsa V (2020) Dynamic functional connectivity between order and randomness and its evolution across the human adult lifespan. Neuroimage 222:117156.

Beggs JM, Plenz D (2003) Neuronal avalanches in neocortical circuits. J Neurosci 23:11167–11177.

Beggs JM, Timme N (2012) Being critical of criticality in the brain. Front Physiol 3:163.

Beim Graben P, Jimenez-Marin A, Diez I, Cortes JM, Desroches M, Rodrigues S (2019) Metastable resting state brain dynamics. Front Comput Neurosci 13:62.

Betzel RF, Bassett DS (2017) Multi-scale brain networks. Neuroimage 160:73–83.

Boly M, Perlbarg V, Marrelec G, Schabus M, Laureys S, Doyon J, Pélégrini-Issac M, Maquet P, Benali H (2012) Hierarchical clustering of brain activity during human nonrapid eye movement sleep. Proc Natl Acad Sci USA 109:5856–5861.

Buzsáki G (2010) Neural syntax: cell assemblies, synapsembles, and readers. Neuron 68:362–385.

Cifre I, Zarepour M, Horovitz SG, Cannas S, Chialvo DR (2017) On why a few points suffice to describe spatiotemporal large-scale brain dynamics. arXiv 1707.00759.

Cocchi L, Gollo LL, Zalesky A, Breakspear M (2017) Criticality in the brain: a synthesis of neurobiology, models and cognition. Prog Neurobiol 158:132–152.

Coombes S, Byrne Á (2019) Next generation neural mass models. In: Nonlinear dynamics in computational neuroscience, pp 1–16. New York: Springer International Publishing.

Cossart R, Aronov D, Yuste R (2003) Attractor dynamics of network up states in the neocortex. Nature 423:283–288.

Damaraju E, Allen EA, Belger A, Ford JM, McEwen S, Mathalon DH, Mueller BA, Pearlson GD, Potkin SG, Preda A, Turner JA, Vaidya JG, van Erp TG, Calhoun VD (2014) Dynamic functional connectivity analysis reveals transient states of dysconnectivity in schizophrenia. Neuroimage Clin 5:298–308.

Deco G, Jirsa VK (2012) Ongoing cortical activity at rest: criticality, multistability, and ghost attractors. J Neurosci 32:3366–3375.

Deco G, Kringelbach ML, Jirsa VK, Ritter P (2017) The dynamics of resting fluctuations in the brain: metastability and its dynamical cortical core. Sci Rep 7:1–14.

Desikan RS, Ségonne F, Fischl B, Quinn BT, Dickerson BC, Blacker D, Buckner RL, Dale AM, Maguire RP, Hyman BT, Albert MS, Killiany RJ (2006) An automated labeling system for subdividing

the human cerebral cortex on MRI scans into gyral based regions of interest. Neuroimage 31:968–980.
Du Y, Pearlson GD, Lin D, Sui J, Chen J, Salman M, Tamminga CA, Ivleva EI, Sweeney JA, Keshavan MS, Clementz BA, Bustillo J, Calhoun VD (2017) Identifying dynamic functional connectivity biomarkers using GIG-ICA: application to schizophrenia, schizoaffective disorder, and psychotic bipolar disorder. Hum Brain Mapp 38:2683–2708.
Dumont G, Gutkin B (2019) Macroscopic phase resetting-curves determine oscillatory coherence and signal transfer in inter-coupled neural circuits. PLoS Comput Biol 15:e1007019.
El-Baba M, Lewis DJ, Fang Z, Owen AM, Fogel SM, Morton JB (2019) Functional connectivity dynamics slow with descent from wakefulness to sleep. PLoS One 14:e0224669.
Engel TA, Steinmetz NA, Gieselmann MA, Thiele A, Moore T, Boahen K (2016) Selective modulation of cortical state during spatial attention. Science 354:1140–1144.
Faskowitz J, Esfahlani FZ, Jo Y, Sporns O, Betzel RF (2020) Edge-centric functional network representations of human cerebral cortex reveal overlapping system-level architecture. Nat Neurosci 23:1644–1654.
Fox MD, Raichle ME (2007) Spontaneous fluctuations in brain activity observed with functional magnetic resonance imaging. Nat Rev Neurosci 8:700–711.
Friston KJ, Mechelli A, Turner R, Price CJ (2000) Nonlinear responses in fMRI: the balloon model, volterra kernels, and other hemodynamics. Neuroimage 12:466–477.
Gast R, Schmidt H, Knösche TR (2020) A mean-field description of bursting dynamics in spiking neural networks with short-term adaptation. Neural Comput 32:1615–1634.
Ghosh A, Rho Y, McIntosh AR, Kötter R, Jirsa VK (2008) Noise during rest enables the exploration of the brain's dynamic repertoire. PLoS Comput Biol 4:e1000196.
Gonzalez-Castillo J, Bandettini PA (2018) Task-based dynamic functional connectivity: recent findings and open questions. Neuroimage 180:526–533.
Gozzi A, Schwarz AJ (2016) Large-scale functional connectivity networks in the rodent brain. Neuroimage 127:496–509.
Grandjean J (2020) A common mouse fMRI resource through unified preprocessing. Radboud University. Available at https://data.donders.ru.nl/collections/di/dcmn/DSC_4180000.18_502.
Grandjean J, Preti MG, Bolton TAW, Buerge M, Seifritz E, Pryce CR, Van De Ville D, Rudin M (2017) Dynamic reorganization of intrinsic functional networks in the mouse brain. Neuroimage 152:497–508.
Grandjean J, Canella C, Anckaerts C, Ayrancı G, Bougacha S, Bienert T, Buehlmann D, Coletta L, Gallino D, Gass N, Garin CM, Nadkarni NA, Hübner NS, Karatas M, Komaki Y, Kreitz S, Mandino F, Mechling AE, Sato C, Sauer K, et al. (2020) Common functional networks in the mouse brain revealed by multi-centre resting-state fMRI analysis. Neuroimage 205:116278.
Gutierrez-Barragan D, Basson MA, Panzeri S, Gozzi A (2019) Infraslow state fluctuations govern spontaneous fMRI network dynamics. Curr Biol 29:2295–2306.e5.
Hansen EC, Battaglia D, Spiegler A, Deco G, Jirsa VK (2015) Functional connectivity dynamics: modeling the switching behavior of the resting state. Neuroimage 105:525–535.
Hindriks R, Adhikari MH, Murayama Y, Ganzetti M, Mantini D, Logothetis NK, Deco G (2016) Can sliding-window correlations reveal dynamic functional connectivity in resting-state fMRI? Neuroimage 127:242–256.
Houweling AR, Brecht M (2008) Behavioural report of single neuron stimulation in somatosensory cortex. Nature 451:65–68.
Huber D, Petreanu L, Ghitani N, Ranade S, Hromádka T, Mainen Z, Svoboda K (2008) Sparse optical microstimulation in barrel cortex drives learned behaviour in freely moving mice. Nature 451:61–64.
Hutchison RM, Womelsdorf T, Allen EA, Bandettini PA, Calhoun VD, Corbetta M, Della Penna S, Duyn JH, Glover GH, Gonzalez-Castillo J, Handwerker DA, Keilholz S, Kiviniemi V, Leopold DA, de Pasquale F, Sporns O, Walter M, Chang C (2013) Dynamic functional connectivity: promise, issues, and interpretations. Neuroimage 80:360–378.
Jercog D, Roxin A, Barthó P, Luczak A, Compte A, de la Rocha J (2017) UP-DOWN cortical dynamics reflect state transitions in a bistable network. Elife 6:e22425.
Jirsa VK, Proix T, Perdikis D, Woodman MM, Wang H, Gonzalez-Martinez J, Bernard C, Bénar C, Guye M, Chauvel P, Bartolomei F (2017) The virtual epileptic patient: individualized whole-brain models of epilepsy spread. Neuroimage 145:377–388.
Karahanoğlu FI, Van De Ville D (2015) Transient brain activity disentangles fMRI resting-state dynamics in terms of spatially and temporally overlapping networks. Nat Commun 6:1–10.
Karsai M, Kaski K, Barabási AL, Kertész J (2012) Universal features of correlated bursty behaviour. Sci Rep 2:397–397.
Kuramoto Y (2003) Chemical oscillations, waves, and turbulence. North Chelmsford: Courier Corporation.
Laing CR (2017) Phase oscillator network models of brain dynamics. In: Computational models of brain and behavior, pp 505–517. Hoboken: Wiley.
Larson-Prior LJ, Zempel JM, Nolan TS, Prior FW, Snyder AZ, Raichle ME (2009) Cortical network functional connectivity in the descent to sleep. Proc Natl Acad Sci USA 106:4489–4494.
Laumann TO, Snyder AZ, Mitra A, Gordon EM, Gratton C, Adeyemo B, Gilmore AW, Nelson SM, Berg JJ, Greene DJ, McCarthy JE, Tagliazucchi E, Laufs H, Schlaggar BL, Dosenbach NUF, Petersen SE (2017) On the stability of BOLD fMRI correlations. Cereb Cortex 27:4719–4732.
Liégeois R, Laumann TO, Snyder AZ, Zhou J, Yeo BT (2017) Interpreting temporal fluctuations in resting-state functional connectivity MRI. Neuroimage 163:437–455.
Lindquist MA, Xu Y, Nebel MB, Caffo BS (2014) Evaluating dynamic bivariate correlations in resting-state fMRI: a comparison study and a new approach. Neuroimage 101:531–546.
Liu X, Duyn JH (2013) Time-varying functional network information extracted from brief instances of spontaneous brain activity. Proc Natl Acad Sci USA 110:4392–4397.
Lombardo D, Cassé-Perrot C, Ranjeva JP, Le Troter A, Guye M, Wirsich J, Payoux P, Bartrés-Faz D, Bordet R, Richardson JC, Felician O, Jirsa V, Blin O, Didic M, Battaglia D (2020) Modular slowing of resting-state dynamic functional connectivity as a marker of cognitive dysfunction induced by sleep deprivation. Neuroimage 222:117155.
Lu H, Zou Q, Gu H, Raichle ME, Stein EA, Yang Y (2012) Rat brains also have a default mode network. Proc Natl Acad Sci USA 109:3979–3984.
Luczak A, Barthó P, Marguet SL, Buzsáki G, Harris KD (2007) Sequential structure of neocortical spontaneous activity in vivo. Proc Natl Acad Sci USA 104:347–352.
Majeed W, Magnuson M, Hasenkamp W, Schwarb H, Schumacher EH, Barsalou L, Keilholz SD (2011) Spatiotemporal dynamics of low frequency BOLD fluctuations in rats and humans. Neuroimage 54:1140–1150.
Mandino F, Yun YL, Gigg J, Olivo MC, Grandjean J (2019) Mouse rest 3 x TG. Openneuro. Available at https://openneuro.org/datasets/ds001890/versions/1.0.1.
Marder E, Taylor AL (2011) Multiple models to capture the variability in biological neurons and networks. Nat Neurosci 14:133–138.
Medic G, Wille M, Hemels ME (2017) Short- and long-term health consequences of sleep disruption. Nat Sci Sleep 9:151–161.
Melozzi F, Woodman MM, Jirsa VK, Bernard C (2017) The virtual mouse brain: a computational neuroinformatics platform to study whole mouse brain dynamics. eNeuro 4:ENEURO.0111-17.2017.
Melozzi F, Bergmann E, Harris JA, Kahn I, Jirsa V, Bernard C (2019) Individual structural features constrain the mouse functional connectome. Proc Natl Acad Sci USA 116:26961–26969.
Montbrió E, Pazó D, Roxin A (2015) Macroscopic description for networks of spiking neurons. Phys Rev X 5:e021028.
Monto S, Palva S, Voipio J, Palva JM (2008) Very slow EEG fluctuations predict the dynamics of stimulus detection and oscillation amplitudes in humans. J Neurosci 28:8268–8272.

Oh SW, Harris JA, Ng L, Winslow B, Cain N, Mihalas S, Wang Q, Lau C, Kuan L, Henry AM, Mortrud MT, Ouellette B, Nguyen TN, Sorensen SA, Slaughterbeck CR, Wakeman W, Li Y, Feng D, Ho A, Nicholas E, et al. (2014) A mesoscale connectome of the mouse brain. Nature 508:207–214.

Ott E, Antonsen TM (2008) Low dimensional behavior of large systems of globally coupled oscillators. Chaos 18:e037113.

Plenz D, Kitai ST (1998) Up and down states in striatal medium spiny neurons simultaneously recorded with spontaneous activity in fast-spiking interneurons studied in cortex–striatum–substantia nigra organotypic cultures. J Neurosci 18:266–283.

Ponce-Alvarez A, Deco G, Hagmann P, Romani GL, Mantini D, Corbetta M (2015) Resting-state temporal synchronization networks emerge from connectivity topology and heterogeneity. PLoS Comput Biol 11:e1004100.

Pope M, Fukushima M, Betzel R, Sporns O (2021) Modular origins of high-amplitude co-fluctuations in fine-scale functional connectivity dynamics. bioRxiv 2021.05.16.444357.

Power JD, Cohen AL, Nelson SM, Wig GS, Barnes KA, Church JA, Vogel AC, Laumann TO, Miezin FM, Schlaggar BL, Petersen SE (2011) Functional network organization of the human brain. 72:665–678. Neuron

Preti MG, Van De Ville D (2017) Dynamics of functional connectivity at high spatial resolution reveal long-range interactions and fine-scale organization. Sci Rep 7:1–12.

Preti MG, Bolton TA, Van De Ville D (2017) The dynamic functional connectome: state-of-the-art and perspectives. Neuroimage 160:41–54.

Prichard D, Theiler J (1994) Generating surrogate data for time series with several simultaneously measured variables. Phys Rev Lett 73:951–954.

Qin J, Chen SG, Hu D, Zeng LL, Fan YM, Chen XP, Shen H (2015) Predicting individual brain maturity using dynamic functional connectivity. Front Hum Neurosci 9:418.

Rashid B, Damaraju E, Pearlson GD, Calhoun VD (2014) Dynamic connectivity states estimated from resting fMRI identify differences among schizophrenia, bipolar disorder, and healthy control subjects. Front Hum Neurosci 8:897.

Sanz Leon P, Knock SA, Woodman MM, Domide L, Mersmann J, McIntosh AR, Jirsa V (2013) The virtual brain: a simulator of primate brain network dynamics. Front Neuroinform 7:10.

Sanz-Leon P, Knock SA, Spiegler A, Jirsa VK (2015) Mathematical framework for large-scale brain network modeling in the virtual brain. Neuroimage 111:385–430.

Scheffer M, Bascompte J, Brock WA, Brovkin V, Carpenter SR, Dakos V, Held H, van Nes EH, Rietkerk M, Sugihara G (2009) Early-warning signals for critical transitions. Nature 461:53–59.

Schirner M (2018) Hybrid brain model data. OSF. Available at osf.io/mndt8.

Schirner M, Rothmeier S, Jirsa VK, McIntosh AR, Ritter P (2015) An automated pipeline for constructing personalized virtual brains from multimodal neuroimaging data. Neuroimage 117:343–357.

Schirner M, McIntosh AR, Jirsa V, Deco G, Ritter P (2018) Inferring multi-scale neural mechanisms with brain network modelling. Elife 7:e28927.

Sforazzini F, Schwarz AJ, Galbusera A, Bifone A, Gozzi A (2014) Distributed BOLD and CBV-weighted resting-state networks in the mouse brain. Neuroimage 87:403–415.

Shine JM, Koyejo O, Bell PT, Gorgolewski KJ, Gilat M, Poldrack RA (2015) Estimation of dynamic functional connectivity using multiplication of temporal derivatives. Neuroimage 122:399–407.

Shine JM, Bissett PG, Bell PT, Koyejo O, Balsters JH, Gorgolewski KJ, Moodie CA, Poldrack RA (2016) The dynamics of functional brain networks: integrated network states during cognitive task performance. Neuron 92:544–554.

Smith SM, Miller KL, Moeller S, Xu J, Auerbach EJ, Woolrich MW, Beckmann CF, Jenkinson M, Andersson J, Glasser MF, Van Essen DC, Feinberg DA, Yacoub ES, Ugurbil K (2012) Temporally-independent functional modes of spontaneous brain activity. Proc Natl Acad Sci USA 109:3131–3136.

Stafford JM, Jarrett BR, Miranda-Dominguez O, Mills BD, Cain N, Mihalas S, Lahvis GP, Lattal KM, Mitchell SH, David SV, Fryer JD, Nigg JT, Fair DA (2014) Large-scale topology and the default mode network in the mouse connectome. Proc Natl Acad Sci USA 111:18745–18750.

Steriade M, Nunez A, Amzica F (1993) A novel slow (<1 Hz) oscillation of neocortical neurons in vivo: depolarizing and hyperpolarizing components. J Neurosci 13:3252–3265.

Su J, Shen H, Zeng LL, Qin J, Liu Z, Hu D (2016) Heredity characteristics of schizophrenia shown by dynamic functional connectivity analysis of resting-state functional MRI scans of unaffected siblings. Neuroreport 27:843–848.

Tagliazucchi E, Balenzuela P, Fraiman D, Chialvo DR (2012a) Criticality in large-scale brain fMRI dynamics unveiled by a novel point process analysis. Front Physiol 3:15.

Tagliazucchi E, Von Wegner F, Morzelewski A, Brodbeck V, Laufs H (2012b) Dynamic BOLD functional connectivity in humans and its electrophysiological correlates. Front Hum Neurosci 6:339.

Tagliazucchi E, Crossley N, Bullmore ET, Laufs H (2016) Deep sleep divides the cortex into opposite modes of anatomical–functional coupling. Brain Struct Funct 221:4221–4234.

Taher H, Torcini A, Olmi S (2020) Exact neural mass model for synaptic-based working memory. PLoS Comput Biol 16:e1008533.

Upadhyay J, Baker SJ, Chandran P, Miller L, Lee Y, Marek GJ, Sakoglu U, Chin CL, Luo F, Fox GB, Day M (2011) Default-mode-like network activation in awake rodents. PLoS One 6:e27839.

van den Heuvel MP, Sporns O (2013) Network hubs in the human brain. Trends Cogn Sci 17:683–696.

Vincent JL, Patel GH, Fox MD, Snyder AZ, Baker JT, Van Essen DC, Zempel JM, Snyder LH, Corbetta M, Raichle ME (2007) Intrinsic functional architecture in the anaesthetized monkey brain. Nature 447:83–86.

Vyazovskiy VV, Olcese U, Hanlon EC, Nir Y, Cirelli C, Tononi G (2011) Local sleep in awake rats. Nature 472:443–447.

Zamani Esfahlani F, Jo Y, Faskowitz J, Byrge L, Kennedy DP, Sporns O, Betzel RF (2020) High-amplitude cofluctuations in cortical activity drive functional connectivity. Proc Natl Acad Sci USA 117:28393–28401.